JGR Solid Earth

RESEARCH ARTICLE
10.1029/2024JB029099

Multiple Seismic Slip-Rate Pulses and Mechanical and Textural Evolution of Calcite-Bearing Fault Gouges

C. Cornelio[1], S. Aretusini[1], E. Spagnuolo[1], G. Di Toro[1,2], and M. Cocco[1]

[1]Sezione di Roma 1, Istituto Nazionale di Geofisica e Vulcanologia, Roma, Italy, [2]Dipartimento di Geoscienze, Università degli Studi di Padova, Padova, Italy

Key Points:

- Friction experiments applying up to four consecutive seismic slip-rate pulses (1 m/s), in fault gouge and bare-rock surfaces
- The greatest changes in dissipated energy occurred between the first and the second slip-rate pulse
- Strain localization in the principal slip zones minimizes the energy dissipated within the whole experimental fault zone

Supporting Information:

Supporting Information may be found in the online version of this article.

Correspondence to:

C. Cornelio,
chiara.cornelio@ingv.it

Citation:

Cornelio, C., Aretusini, S., Spagnuolo, E., Di Toro, G., & Cocco, M. (2024). Multiple seismic slip-rate pulses and mechanical and textural evolution of calcite-bearing fault gouges. *Journal of Geophysical Research: Solid Earth*, *129*, e2024JB029099. https://doi.org/10.1029/2024JB029099

Received 13 MAR 2024
Accepted 20 JUN 2024

Author Contributions:

Conceptualization: C. Cornelio, E. Spagnuolo
Funding acquisition: M. Cocco
Investigation: C. Cornelio, S. Aretusini, G. Di Toro
Methodology: C. Cornelio, S. Aretusini
Validation: S. Aretusini
Visualization: C. Cornelio
Writing – original draft: C. Cornelio
Writing – review & editing: S. Aretusini, E. Spagnuolo, G. Di Toro, M. Cocco

Abstract Natural fault zones are complex, spatially heterogeneous systems. Rock deformation experimental studies simplify the complexity of natural fault zones either as a surface discontinuity between intact rocks (bare-rock surfaces) or as a few mm-thick gouge layer. However, depending on the simplified fault type and its slip history, the response to applied deformation can vary. In this work, we conduct laboratory experiments for investigating the evolution of mechanical parameters of simulated faults made of calcite gouge subjected to multiple (four) identical seismic slip-rate pulses. We observed that, as the number of applied slip-rate pulses increased, (a) initial friction and steady-state friction remained approximatively constant, (b) peak friction and normalized strength excess increased and, (c) the slip distances to achieve peak and steady-state friction, D_a and D_c, decreased. The greatest changes occurred between the first and the second slip-rate pulse. From this pulse onward, the dissipated energy of the calcite gouge fault was similar to those obtained in bare-rock surfaces experiments. Microstructural analysis showed that, strain is localized in up to two (recrystallized) principal slip zones (PSZ) with sub-micrometric grain size, surrounded by low porosity sintered and non-sintered comminuted gouge domains. We conclude that previous seismic slip episodes impact on both the structure and the strain localization processes within a fault, contributing to its shear fabric evolution. We highlight that the strain localization process identifies the PSZ, dissipating the least amount of energy within the entire experimental fault zone.

Plain Language Summary Earthquakes are caused by the propagation of seismic ruptures and sliding of rocks along geological structures called faults. Within the fault, seismic ruptures propagate in mm-cm thick slip zones that cut cm- to meters-thick fault cores. Both slip zones and fault cores typically exhibit microstructural assemblages different from those of nearby rocks. Laboratory experiments are used to investigate the processes that result in the decrease of fault strength with slip and slip-rate and govern seismic rupture propagation. However, experiments are performed on simplified fault cores consisting of either a surface discontinuity between intact rocks (i.e., slip zone = "bare-rock surfaces") or a mm-thick layer of powdered rocks (i.e., slip zone in a "fault gouge"). In this work, we investigate how slip zones form and evolve in an experimental fault (gouge) core depending on seismic slip history. We apply repeated pulses of seismic slip and show that (a) in the first pulse a slip zone with similar microstructure and friction properties to bare-rock is formed, (b) in subsequent pulses these slip zones are abandoned and new slip zones are formed in the fault core. Notably, these structural changes, occur to minimize the mechanical energy dissipated in the FC.

1. Introduction

In the shallow Earth's crust, fault zones are complex systems composed of a distribution of fault rocks with spatially heterogeneous mineralogy, rheology, cohesion, transport, and frictional properties (Caine et al., 1996; Faulkner et al., 2010). The primary components of a fault zone are the fault core (FC) (often more than one), the damage zone (DZ), and the intact protolith or host rock (Caine et al., 1996; Chester & Logan, 1986; Faulkner et al., 2010). The FC is the inner portion of the fault zone where most of the displacement is accommodated (Caine et al., 1996). FC includes one or more individual fault slip surfaces separating a thin PSZ (usually <0.1 m thick) (Sibson, 2003; Smith et al., 2011) made of non-cohesive (gouges or rock powders) or cohesive (cataclasites) fragmented rocks (Masoch et al., 2022; Sibson, 1989). The DZ surrounds the FC and typically includes a dense network of fractures, secondary faults, and fold structures (Caine et al., 1996). The structure of a fault zone depends also on its slip history (Sibson, 1977): for instance, immature faults have accommodated lower slip compared to mature fault zones, the latter having well-developed FC with multiple and overprinted PSZs,

surrounded by up to several hundreds of meters thick damage zones (Chester & Chester, 1998; Faulkner et al., 2003; Fondriest et al., 2020).

Natural fault rocks are complex, mainly because they underwent a long geological history comprised of deformation events with variable slip, slip-rate, temperature, shear stress τ and normal stress σ_n plus the exhumation from seismological depths. Moreover, fault zone rocks interact with fluids that might react with the unstable products of coseismic slip (i.e., the nanoparticles), or might determine the precipitation of fault veins, also in multiple events, that might seal (and heal) the PSZs, the FC and the DZ. The FC is also characterized by the formation of several PSZs likely indicating multiple seismic events (Collettini et al., 2014, 2019; Demurtas et al., 2016; Leah et al., 2018). In natural calcite bearing fault cores, cold sintering (or pressure-solution and mass transfer diffusion), and precipitation of veins from percolating fluids may also contribute to the hardening of the carbonatic gouges in the FC (Chinello et al., 2023; Demurtas et al., 2016).

The frictional properties of faults are investigated in laboratory rock deformation experiments. However, the complexity of natural fault zones is simplified, either as a surface discontinuity between intact rocks (bare-rock experiments) (Dieterich, 1972; Ohnaka, 2003; Ohnaka & Shen, 1999; among others) or as few mm-thick gouge layer sandwiched between metal or rock sample holders (Byerlee, 1978; Dieterich, 1981; Marone, 1998). In particular, rotary shear apparatuses are designed to impose on bare-rock surfaces or gouge layers (usually <5 mm thick) the large fault slip (>0.01 m), the high slip-rate (>0.1 m/s) and the accelerations (>>~10 m/s^2) typical of natural earthquakes of moment magnitude M_w > 3 (Heaton, 1990; Ma et al., 2014). In these so-called "high velocity rock friction experiments" (HVFE), dynamic weakening mechanisms are activated in the experimental faults, leading to the abrupt reduction of fault shear strength (or friction) due to rock dependent deformation processes (Di Toro et al., 2011; Nielsen et al., 2021; Tullis, 2015).

Depending on the type (bare-rock or gouge) of the initial fault material, the frictional response to seismic deformation can vary. In bare-rocks with pre-existing surfaces, strain is already localized and the temperature rise in the slipping zone increases with slip-rate, effective normal stress and square root of the duration of slip (Archard, 1959; Carslaw & Jaeger, 1959; Rice, 2006). In bare-rock surfaces, the abrupt increase in temperature favors the activation of asperity scale processes, such as "flash" heating and weakening (Brantut & Viesca, 2017; Goldsby & Tullis, 2011; Rice, 2006; Spagnuolo et al., 2015). In the case of experiments performed on bare-rock surfaces of calcite-bearing rocks through the application of a seismic slip pulse, the slip zone is extremely thin (<10 μm thick), and made of nano-particles (<100 nm is size) and recrystallized calcite grains bounded by a (mirror-like) slip surface paved by >2–3 μm in size and <100 nm thick recrystallized calcite grains (Spagnuolo et al., 2015; Tisato et al., 2012; Violay et al., 2013). For fault gouges, a longer initial slip is required to achieve strain localization (Beeler & Tullis, 1997; Marone et al., 1990; Platt et al., 2014, 2015; Pozzi et al., 2018; Rempe et al., 2017; Smith et al., 2015). As a consequence, heat production is distributed in the slipping zone and other processes including thermal pressurization (if fluids are already present in the pores of the slipping zone) and thermomechanical pressurization (if fluids like CO_2 and H_2O are released by the breakdown of the minerals of the slipping zone, like calcite or clays) might be favored (Brantut et al., 2008; Ferri et al., 2010; Rempel & Rice, 2006; Rice, 2006). Moreover, calcite gouge layers deformed in HVFE include a narrow (<100 μm) and fine-grained (<1 μm) shear localization zone made of recrystallized calcite cut by a single or multiple (mirror-like) slip surfaces similar to those found in the case of cohesive rocks (De Paola et al., 2011; Fondriest et al., 2013; Han et al., 2010; Pozzi et al., 2018, 2019, 2021; Smith et al., 2013). In conclusion, in the case of calcite-bearing rocks, the different strain localization process in rock gouges compared to bare-rock surfaces corresponds to different mechanical behaviors, although the mineralogy and seismic loading conditions are identical (Smith et al., 2015).

While the physical parameters controlling coseismic fault weakening were studied in depth, as well as the processes of gouge production from a bare-rock surface (Boneh et al., 2013, 2014; Boneh & Reches, 2018; Hirose et al., 2012; Noël et al., 2023; Wang & Scholz, 1994) or to lithification of gouge into a cataclasite, less studies have focused on the evolution of the gouge layers resulting from multiple slip-rate pulses representing successive earthquakes along the same fault (Han et al., 2010; Smith et al., 2015). Smith et al. (2015) analyzed the fabric evolution of the gouge layer during strain localization and its relation with the weakening process of a calcite marble rock using two consecutive seismic slip-rate pulses and focusing on the early stage of strain localization. They found that the gouge layer resheared after a variable holding time has frictional behavior similar to the bare rock sample and that reactivation occur along the cohesive Principal Slip Surface (PSS) that formed during the first seismic pulse, which can be so considered as a critical precursor to dynamic weakening for the calcite gouge

layer. Moreover, Han et al. (2010) showed a decrease of the slip necessary to reach steady state friction in the second slip pulse. Finally, several works focused on the restrengthening and the healing rate after the shearing at coseismic slip-rate of natural gouge (Yao et al., 2013) or gabbro (Mizoguchi et al., 2009) and granite (Bedford et al., 2023). All these works evidenced a rapid healing due to the dissipation of the heat produced during the fault shearing at seismic slip-rates. Moreover, Yao et al. (2013) showed the development of a complex structure due to the migration of the slip zone in the gouge layer and disruption of the previous developed slip zone.

Finally, HVFE yield information about the energy dissipation during the coseismic phase (Nielsen, Spagnuolo, Smith, et al., 2016). For instance, the analysis of thousands of experiments conducted on both bare-rock surfaces and gouge layers, show the increase of the energy dissipated per unit fault surface with simulated sesismic slip (Cocco et al., 2023; Nielsen, Spagnuolo, Violay, et al., 2016), which is determined in the experiments from the shear stress curve evolution with slip, following the definition of Palmer and Rice (1973). However, a comprehensive examination of fractures and other energy sinks in relation to the frictional behavior and the microstructural evolution of gouge layers during a series of simulated seismic slip events, representing a complex and more realistic slip history, is still lacking.

Here we compare mechanical data and microstructures obtained by deforming experimental calcite-bearing faults made of bare-rock surfaces or of gouge layers after imposing one or up to four seismic slip-rate pulses. The objective is to understand the evolution of the mechanical behavior (friction, dissipated energy, etc.) and the microstructures (strain localization, reworking of pre-existing slip zones, etc.) of a FC made of calcite gouge subjected to a complex slip history.

2. Methods

We deformed samples of Carrara marble using the experimental rotary shear machine SHIVA installed in INGV in Rome ((Di Toro et al., 2010), Figure 1a). Carrara marble was chosen as analogue material of the carbonate-bearing rocks which are common in the seismogenic continental crust at shallow depth in the Mediterranean area (Amato et al., 1998; Ben-Menahem, 1991; Chiaraluce et al., 2011). The experiments were performed on both bare-rock surface and gouge layer samples (Figure 1). The bare-rock surface samples were hollow cylinders 30/50 mm internal/external diameter (Figures 1b and 1d) (Nielsen et al., 2012). The gouge starting material was prepared by grinding the same Carrara marble block (99% calcite with minor dolomite (Violay et al., 2013) of the bare-rock surface samples to ensure a similar mineralogical composition. Then, after grinding we sieved the rock powder with grain size <250 μm. The gouges were sheared using a Titanium alloy (similar thermal properties as calcite-bearing rocks (Yao et al., 2016)) sample holder with 14/30 mm internal/external diameter (Figures 1c–1e). To avoid extrusion of the gouge material during shearing, we used an external hollow cylinder and internal cylinder made of Teflon fixed to the sample holder with a screw (Figures 1c and 1e). This sample holder was attached to the rotary column of SHIVA (Figure 1c). Due to the sample assembly, and in particular to the fact that the Teflon parts are attached to the rotary sample holder, the localization of the gouge layer is forced closer to the stationary side (similarly as in (Aretusini et al. (2017)). The gouge layer was prepared using 3 g or 5 g of material, which corresponded to an initial thickness of ca. 3 and 4.5 mm, respectively. All experiments were performed under room humidity conditions and normal stress σ_n = 10, 20, and 30 MPa. We simulated coseismic slip-rate pulses as a trapezoidal function with maximum slip-rate of ∼1 m/s, slip of 0.93 m and an acceleration and deceleration ramp of 6.4 m/s^2. In the bare-rock surface samples experiments, we imposed one slip-rate pulse. In the gouge layer experiments, we imposed up to four slip-rate pulses, with a holding time between slip-rate pulses of 120 s. This holding time was chosen to avoid effect of rapid healing on the gouge material due to temperature increase during sliding (Bedford et al., 2023; Yao et al., 2013) and sufficiently short for the static postseimic healing to not be relevant (Chen et al., 2015). Mechanical data (axial load, torque, axial displacement and angular rotation) were acquired at a frequency between 4 Hz (hold time) and 12.5 kHz (slip-rate pulse). Slip, slip-rate (or velocity) and shear stress were determined using the method outlined in Niemeijer et al. (2011), Tsutsumi and Shimamoto (1997).

Microstructural investigations were performed on post-mortem gouge samples recovered after the experiments performed at σ_n = 20 MPa using 3 g (s1956, s1957, s1958, s1959) and 5 g (s1960, s1961) of material and on bare-rock surface sample recovered after the experiments performed at σ_n = 20 MPa. Deformed gouge layers and the bare-rock surface sample were embedded in epoxy resin, cut perpendicular to the slip surfaces and tangential to the slip vector, cross-sectioned (Figures 4a, 4b, 5a, and 5b) and polished with Syton. The polished surfaces were

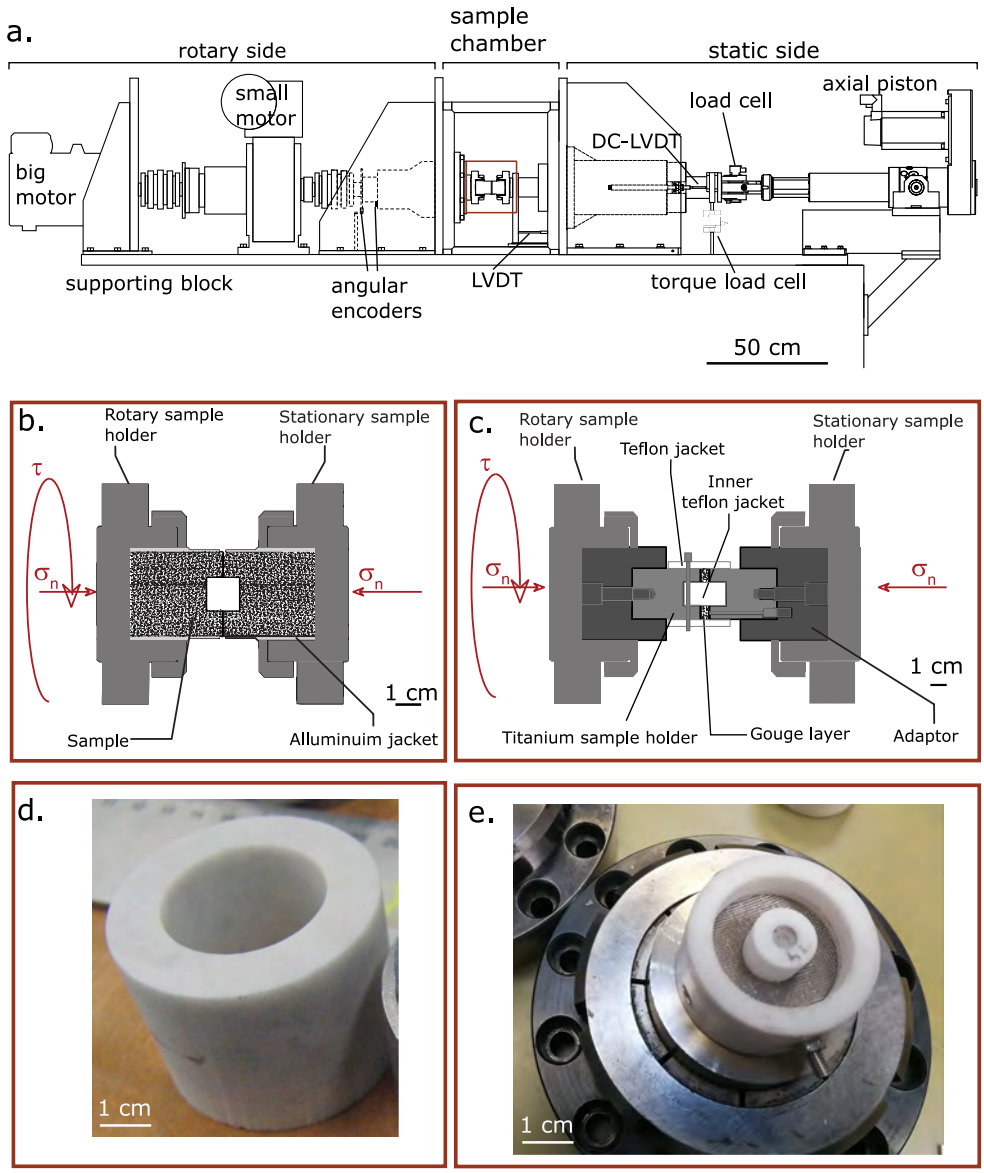

Figure 1. Experimental set-up. (a) Sketch of the rotary shear apparatus SHIVA (modified from Aretusini et al., 2021). (b) Zoom of the sample assembly for bare-rock surface experiments. (c) Zoom of the sample assembly for the gouge layer experiments. (d) Picture of the bare-rock surface sample made of Carrara marble and (e) picture of the gouge sample holder before pouring the gouge layer of Carrara marble.

imaged using a field emission scanning electron microscope (FEG-SEM, JEOL JSM-6500F at INGV, Rome and SEM Tescan Solaris S9252G at Padua University. The working conditions of the FEG-SEM to obtain back-scattered electron images were working distance of ca. 10 mm and accelerating voltage of 15 kV for gouge layers (JEOL JSM-6500F), and working distance of ca. 5 mm and accelerating voltage of 10 kV (Tescan Solaris S9252G).

3. Results

3.1. Mechanical Data

From our experiments, we determine the evolution of the apparent friction μ as the ratio between shear stress τ and normal stress σ_n applied on the experimental fault (Figure 2). At the onset of both gouge layer and bare-rock surface experiments, τ acting on the fault increases until the static friction coefficient μ_0 was overcome and slip initiated.

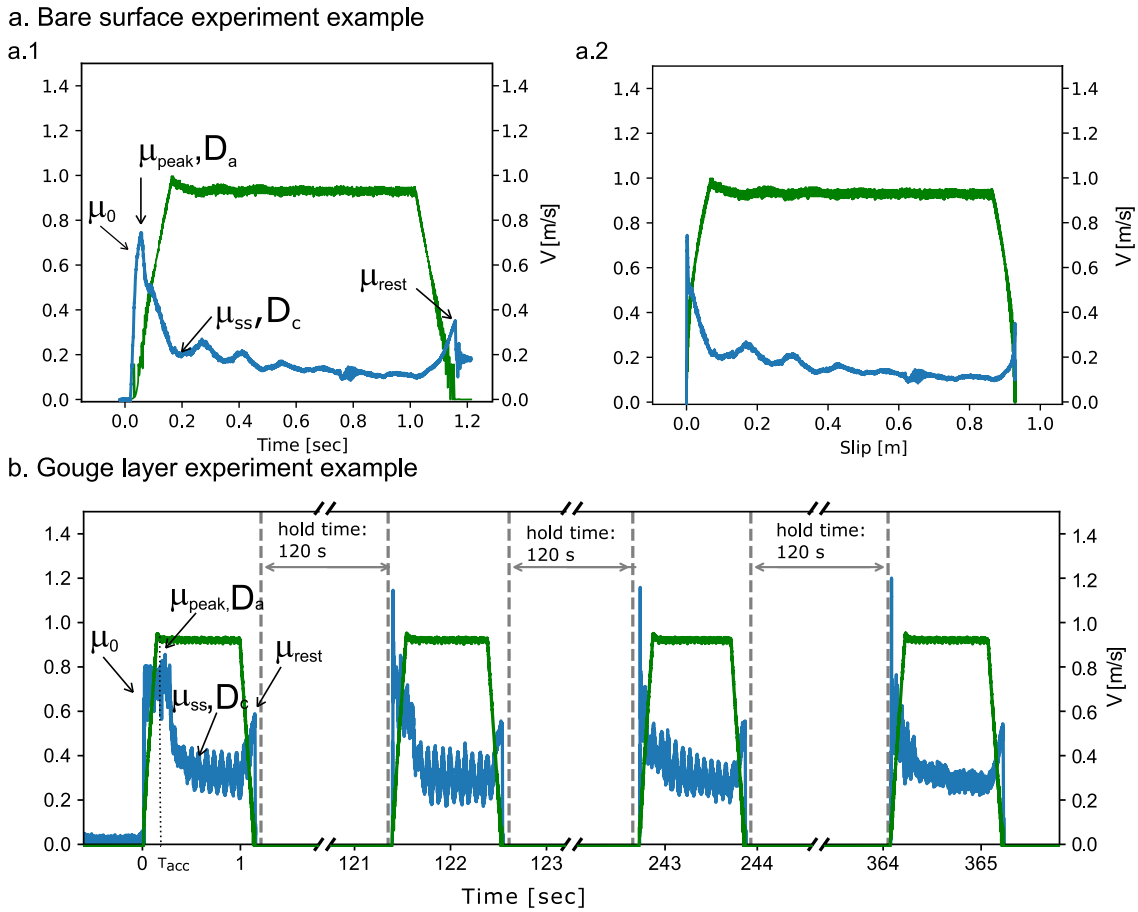

Figure 2. Experimental procedure and definition of the main mechanical parameters. The plots report the evolution of the apparent friction ($\mu = \tau/\sigma_n$, blue curves) and slip-rate (green curves) versus time. In figure are defined the slip weakening distance D_c and the static (μ_0), peak (μ_{peak}), steady-state (μ_{ss}) and restrengthening (μ_{rest}) friction coefficients. (a) Bare-rock surface experiment (s2007 with one seismic slip-rate pulse) versus time (a.1) and versus slip (a.2). (b) Gouge layer experiment (s1863) with four seismic slip-rate pulses separated by a hold time of 120 s.

Immediately after slip initiation, a further increase in μ indicating a slip-strengthening behavior until a peak friction coefficient μ_{peak} over a slip distance D_a is observed. Subsequently, μ decreases up to a "steady-state" dynamic friction coefficient μ_{ss} over a slip distance D_c. The apparent friction evolution with slip distance is fitted following the exponential decay function proposed by Mizoguchi et al. (2007)

$$\mu = \mu_{ss} + (\mu_{peak} - \mu_{ss})\, e^{\ln\left(0.05\ \frac{slip}{D_c}\right)}$$

In our experiments, the achievement of the steady-state friction coefficient requires slip distance of several millimeters to tens of centimeters depending on the type of fault (bare-rock surface or gouge, compare Figures 2a and 2b) and number of slip-rate pulses (Table S1 in Supporting Information S1). In each pulse, when the imposed slip-rate decreases back to 0 m/s, the apparent friction increases again to the restrengthening value μ_{rest}.

For each slip-rate pulse, we determine the five mechanical parameter described above (i.e., μ_0, μ_{peak}, μ_{ss}, μ_{rest}, and D_c). Hereon, the mechanical parameters are either presented individually, or presented as the average and standard deviation of individual parameters grouped by σ_n (bare-rock surfaces) or by σ_n, number of pulses, and weight (gouge layers). We show the dependence of mechanical parameters with (a) the number of applied slip-rate pulses for experiments performed with the gouge layer, (b) the type of fault (bare-rock surface vs. gouge layer), (c) initial weight or thickness of the gouge layer, and (d) the applied σ_n (Figure 3 and Figure S1 in Supporting Information S1). Independently of the number of slip-rate pulses, σ_n, and gouge layer weight, μ_0 is

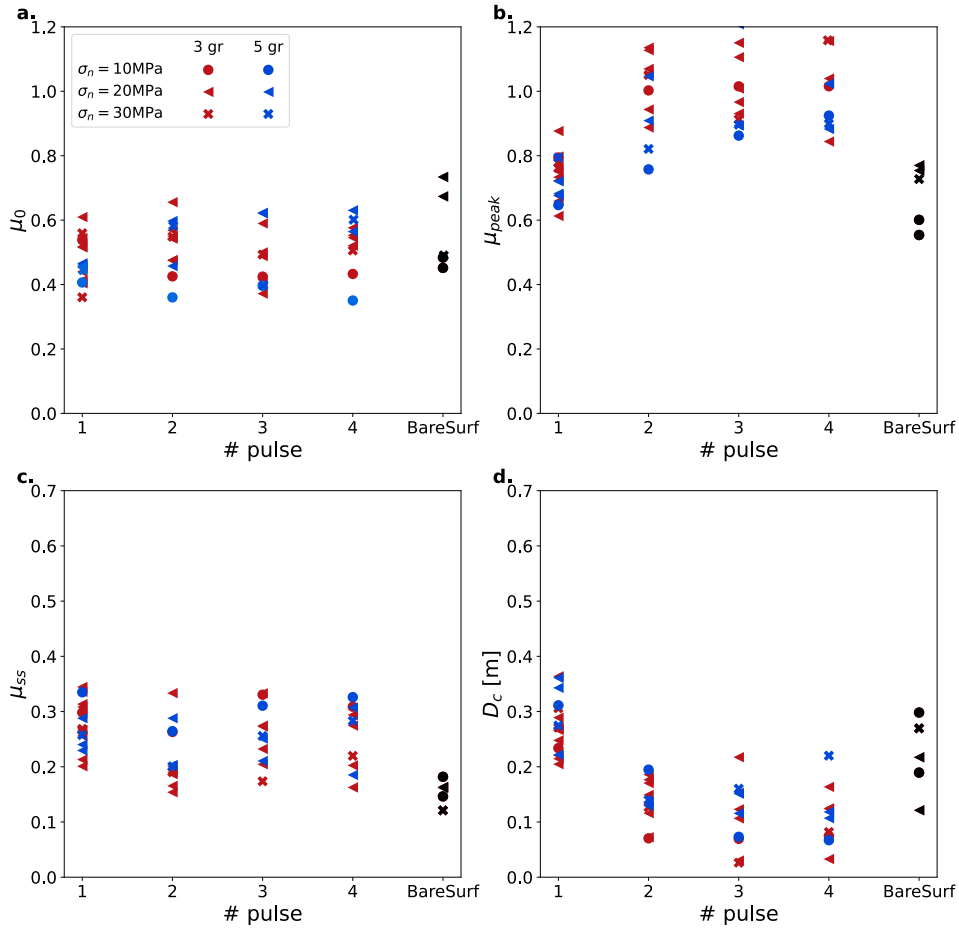

Figure 3. Friction coefficients μ_0, μ_{peak}, μ_{ss} and slip weakening distance D_c (see Figure 2 for their definition) versus number of slip-rate pulses, fault type (gouge layer vs. bare-rock surface), applied normal stress σ_n and initial gouge layer weight (or thickness). (a) Static friction coefficient, (b) peak friction coefficients, (c) steady state friction coefficient, and (d) slip weakening distance D_c.

slightly lower for gouge layer experiments, 0.50 ± 0.08, than in bare-rock surface experiments, 0.53 ± 0.13 (Figure 3a). In the experiments performed on the gouge layers, μ_{peak} increases from 0.74 ± 0.07 at the first slip-rate pulse to 1.02 ± 0.12 at the fourth slip-rate pulse (Figure 3b). The μ_{peak} values are systematically higher than the one measured in bare-rock surface experiments (0.70 ± 0.13, Figure 3b). μ_{ss} in the gouge layer experiments are similar in all the applied slip-rate pulses, though slightly larger in the first pulse but still within the standard deviation (i.e., in order of applied slip-rate pulse: 0.28 ± 0.04, 0.22 ± 0.05, 0.26 ± 0.05, and 0.26 ± 0.06) (Figure 3c). Instead, the average values of μ_{ss} measured in the experiments performed on gouge layers, 0.25 ± 0.05, is higher than the one measured in bare-rocks surface samples, 0.154 ± 0.02 (Figure 3c). Finally, μ_{rest} is independent of the number of slip-rate pulses (0.46 ± 0.11), but higher in gouge layer than in bare-rock surface (0.34 ± 0.03) experiments (Figure S1 in Supporting Information S1). In the layer gouge experiments, D_c drastically decreases from the first, 0.27 ± 0.05 m, to the second slip-rate pulse, 0.14 ± 0.04 m, and then remains constant during the other slip-rate pulses, 0.11 ± 0.06 m and 0.11 ± 0.05 m for the third and fourth pulses, respectively (Figure 3d).

With respect to the experiments performed on bare-rock surfaces (Figure 2a), the gouge layer shows a phase of strengthening at the start of the first slip-rate pulse (Smith et al., 2015) (Figure 2b). In the gouge layer experiments, during the first slip-rate pulse, the slip distance D_a required to overcome μ_{peak} and initiate dynamic weakening decreases with the increase of σ_n from 0.07 m at 10 MPa to 0.025 m at 30 MPa. In the other slip-rate pulses, similarly as in the experiments performed on bare-rock surfaces, D_a is ca. 0.001 m independently of the imposed σ_n (Figure S2 in Supporting Information S1).

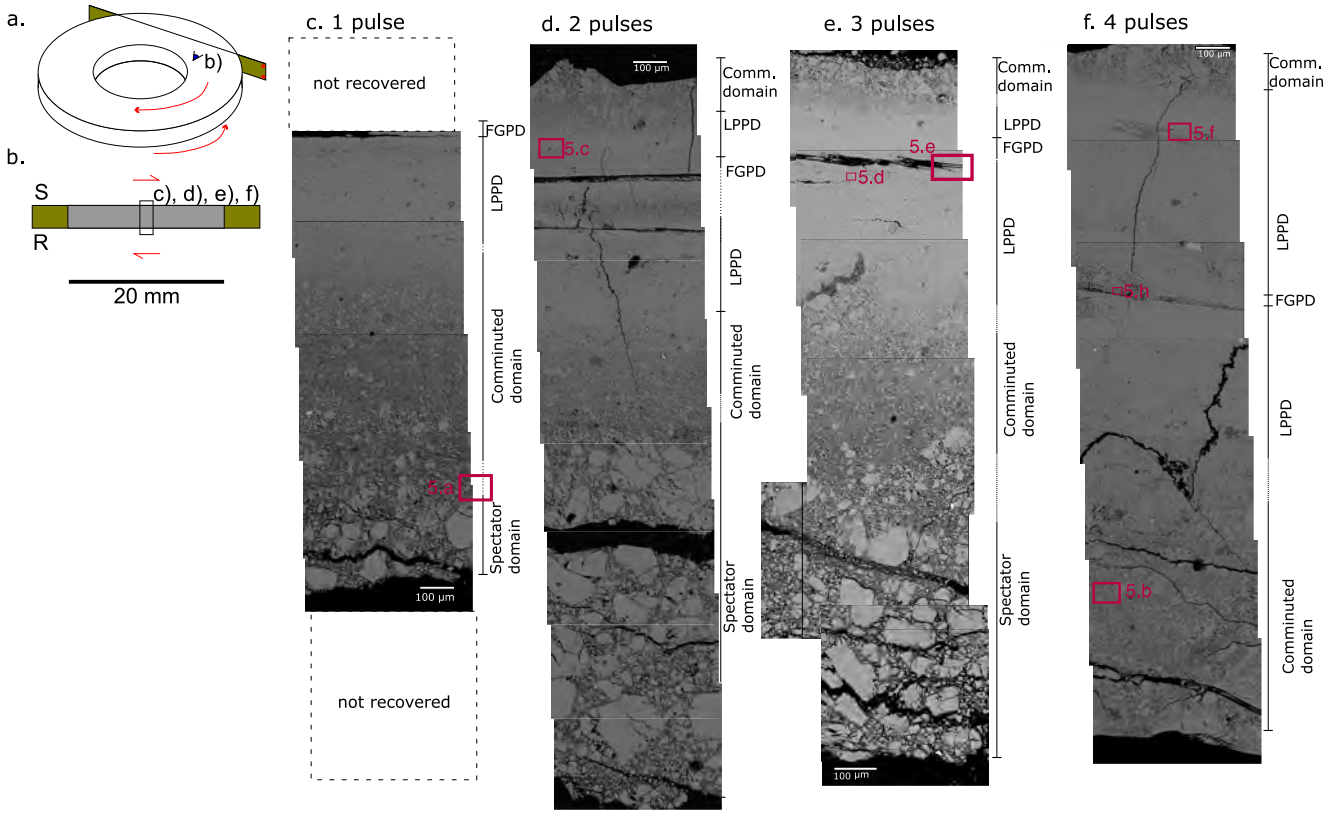

Figure 4. Cross sections of the gouge layers (initial weight 3 g) recovered after the experiments performed at 20 MPa normal stress (SEM-BSE images). (a) Sketch of the sample; (b) sketch of the analyzed section: S stationary side, to the top; R rotary side, to the bottom. (c) Gouge layer after one seismic slip-rate pulse (s1956), (d) after two seismic slip-rate pulses (s1959), (e) three seismic slip-rate pulses (s1958) and (f) four seismic slip-rate pulses (s1957). In all the cross sections, it was possible to recognize four domains: spectator, comminuted, low porosity polygonal (Low porosity polygonal domain) and fine-grained polygonal (Fine-grained polygonal domain) domains. The latter is interpreted to be the principal slip zone (principal slip zones|principal slipping zone, see main text and Figure 5).

3.2. Microstructural Evolution With Subsequent Slip-Rate Pulses

After the experiments, the gouge layer became in part cohesive, and a complete recovery of the gouge layer was possible after two or more applied slip-rate pulses. However, after the first slip-rate pulse, loose material was still present and not easily recoverable.

By observing SEM-BSE images of the gouge layers sheared at σ_n of 20 MPa and recovered after one (Figure 4c and Figure S2a in Supporting Information S1), two (Figure 4d), three (Figure 4e) or four (Figure 4f and Figure S2b in Supporting Information S1) slip-rate pulses, we recognize the following microstructural domains:

1. **"Spectator domain"**: poorly deformed (mainly by compaction (Rempe et al., 2020)) gouge layer with grain size <250 µm and very similar to the starting calcite gouge. Calcite grains have straight boundaries and fracture along cleavage planes (e.g., Figure 5a).
2. **"Comminuted domain"**: deformed gouge (mainly by shear, Rempe et al., 2020) layer with grain size ranging from <1 µm to ca. 50 µm resembling common cataclasites (e.g., Demurtas et al., 2016). The calcite grains have sharp to arcuate-lobate boundaries, possibly due to spallation, indentation and fragmentation processes (Figure 5b).
3. **"Low porosity polygonal domain (LPPD)"**: deformed and recrystallized gouge layer (mainly by shear, see Smith et al., 2013; Rempe et al., 2020; Pozzi et al., 2018) with grain size ranging from 1 µm to ca. 30 µm and polygonal porous texture resembling calcitic mylonites (Figures 5c and 5d). The calcite grains are euhedral, with straight grain boundaries and incomplete (far from the slip zone) to almost complete (approaching the "fine-grained polygonal domain", see below) triple junctions (Figure 5d). This domain includes few partially decomposed dolomite clasts (Figure 5c). Locally, a gradient of grain size across the domain is recognized, with smaller grains next to principal slip zone (PSZ, Figure 4, see below).

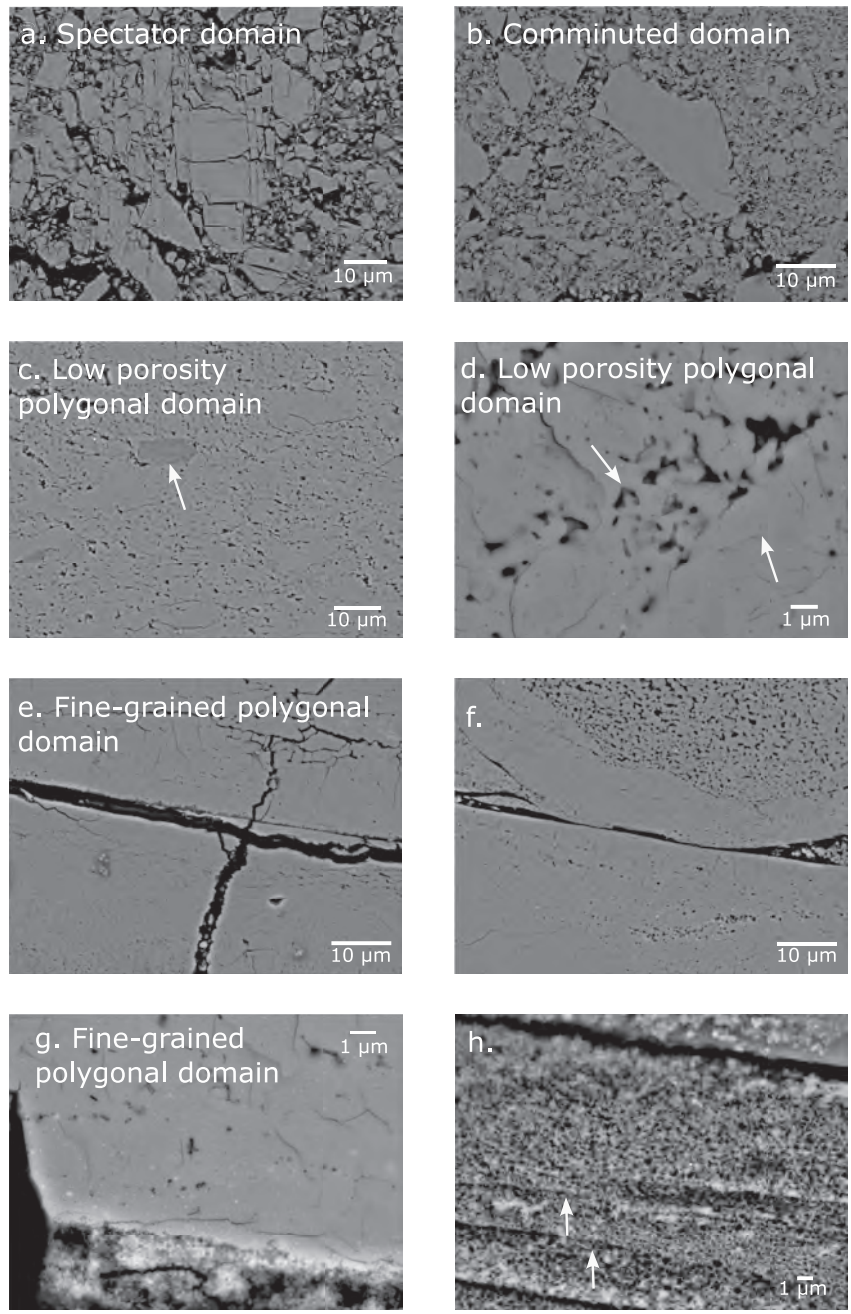

Figure 5. Microstructural domains (FESEM-BSE images). (a) Spectator domain (s1956); (b) Comminuted domain (s1957); (c) Low porosity polygonal domain (LPPD) (s1959). Arrow: dolomite grain; (d) LPPD area with arrows indicating complete and incomplete triple junctions (s1958); (e) Fine-grained polygonal domain (FGPD) (interpreted as principal slip zones| principal slipping zone) cut by an open fracture (s1958); (f) Bent fragment of FGPD bounded by a low porosity domain (top side) and by a continuous sharp ultra-polished fracture and a FGPD (bottom) (s1957); (g) FGPD bounded at the bottom by a very porous layer made of calcite grains <200 nm in size (or "nano-particles"); (h) Spatial arrangement of the nano-particles of calcite with Y-type fractures (white arrows).

4. **"Fine-grained polygonal domain (FGPD)"**: deformed and recrystallized gouge layers (mainly by shear) interpreted as PSZs with grain size <1 µm and polygonal texture. As in LPPD, the calcite grains are euhedral and with straight boundaries but the triple junctions are usually complete. The FGPD has a thickness of 20–50 µm (see also Pozzi et al., 2018, 2019, 2021) and is bounded by sharp ultra-polished (mirror-like) continuous

fracture surfaces (Figure 5e, see below). Bent fragments of the FGPD are found next to the sharp ultra-polished and to the healed fractures (Figure 5f).

We also recognize the following microstructural features associated with the presence of fractures, which are often located at grain size contrasts (e.g., boundary between LPPD and the FGPD or PSZ, Figure 5f):

- Sharp ultra-polished (mirror-like) continuous fractures parallel to the slip vector (Pozzi et al., 2018; Smith et al., 2013) filled by rounded calcite grains <200 nm in size (or "nano-particles") cut by Y-type fractures (Logan et al., 1992) (Figures 5g and 5h);
- Sharp ultra-polished open continuous or segmented imbricated fractures. They may lead to fragmentation and rotation of the FGPD (or PSZs, Figure 4d).
- Healed fractures which appear as trails of micropores cutting the LPPD. Locally, healed fractures often bound bent fragments of the FGPD or PSZs (Figure 5f). Healed fractures are sub-parallel to the Y-type and to R-type fractures.

In general, the number and spatial arrangement of the four domains evolves with the number of slip-rate pulses resulting in more complex gouge layer structures. First, the total thickness of the comminuted, LPPDs and FGPDs increases at the expense of the spectator domain with the number of slip-rate pulses from ~550 μm (two slip-rate pulses, s1959) to ~1,330 μm (four slip-rate pulses, s1957) (Figures 4c–4f). Second, the number of FGPDs, interpreted as PSZs, and of the LPPDs, interpreted as gouge volumes next to the PSZ, increases from one after the one slip-rate pulse to at least two after the two and more slip-rate pulses experiments (compare Figure 4c with Figures 4d–4f). Third, the FGPDs and the LPPDs are formed next to the stationary side of the sample assemblage in the first slip-rate pulse and inside the gouge layer, toward the rotary side, in the following slip-rate pulses (compare Figure 4c with Figure 4f). Eventually, in the four slip-rate pulses, the entire gouge layer experienced comminution or recrystallization and the maximum observed grain size is ~50 μm.

We perform microstructural analysis on a bare-rock surface sample recovered from the experiment s2007 performed at 20 MPa normal stress with one seismic slip-rate pulse (Figure 6). The slip surface (Figure 6c) is locally preserved and it is surrounded by microstructural domains identical to those recognized in deformed gouge layers (Figure 5f). Toward the bottom of the slip surface (rotary side), a <15 μm FGPD develops (Figure 6d). The slip zone is made of euhedral to rounded nano-particles (<100 nm is size) of calcite, lime and portlandite locally mixed with amorphous carbon (Spagnuolo et al., 2015; Tisato et al., 2012; Violay et al., 2013) (Figure 6e). To the top of the slip surface and to the bottom of the FGPD domain, a LPPD develops resulting from calcite decarbonation and transitional to the wall rock (e.g., Han et al., 2010; Spagnuolo et al., 2015; Tisato et al., 2012; Violay et al., 2013) (Figures 6d–6f). To the bottom of this is the spectator domain, almost indistinguishable from the original undeformed rock (Figure 6c). Along strike, the PSS is welded and obliterated by the LPPD (Figure 6f). Remarkably, the FGPD in bare-rock surface after one seismic slip-rate pulse (Figure 6e) is very similar to the FGPD in gouge layer after four seismic slip-rate pulses (Figure 5h).

4. Discussion

4.1. Evolution of Mechanical Parameters

The application of repeated slip-rate pulses in gouge layer experiments is performed in this study to analyze the succession of multiple dynamic instabilities in a simulated fault with the aim to discuss the evolution of mechanical parameters represented by friction coefficients (μ_0, μ_{peak}, μ_{ss}, μ_{rest}), slip strengthening and weakening distances (D_a, D_c), dissipated energy and the associated microstructures. The results of experiments with bare-rock surface are used as a reference or end-member configuration of a fault zone with extreme strain localization (see also Cornelio et al., 2022; Nielsen et al., 2021). The values of the initial friction coefficient μ_0 remain nearly constant during the application of repeated slip-rate pulses and independently of the initial gouge layer thickness, with values similar to those measured in experiments performed on bare-rock surfaces (Figure 3a). Differently, the peak friction coefficient μ_{peak} increases at each applied slip-rate pulse becoming higher than 1.0 in some cases (Figure 3b). On average, the thinner experimental fault (with 3 g of gouge material) yields higher values of μ_{peak} than the thicker one (with 5 g of gouge). The μ_{ss} values are higher in the gouge layer experiments than in experiments in bare-rock surfaces, as already observed by Proctor et al. (2014) for serpentinite rich lithology. Moreover, we noticed that: (a) μ_{ss} is not affected by the number of pulses and being larger in gouge than in bare-rock surface experiments; (b) the average values of D_c were larger in gouge than in bare-rock experiments

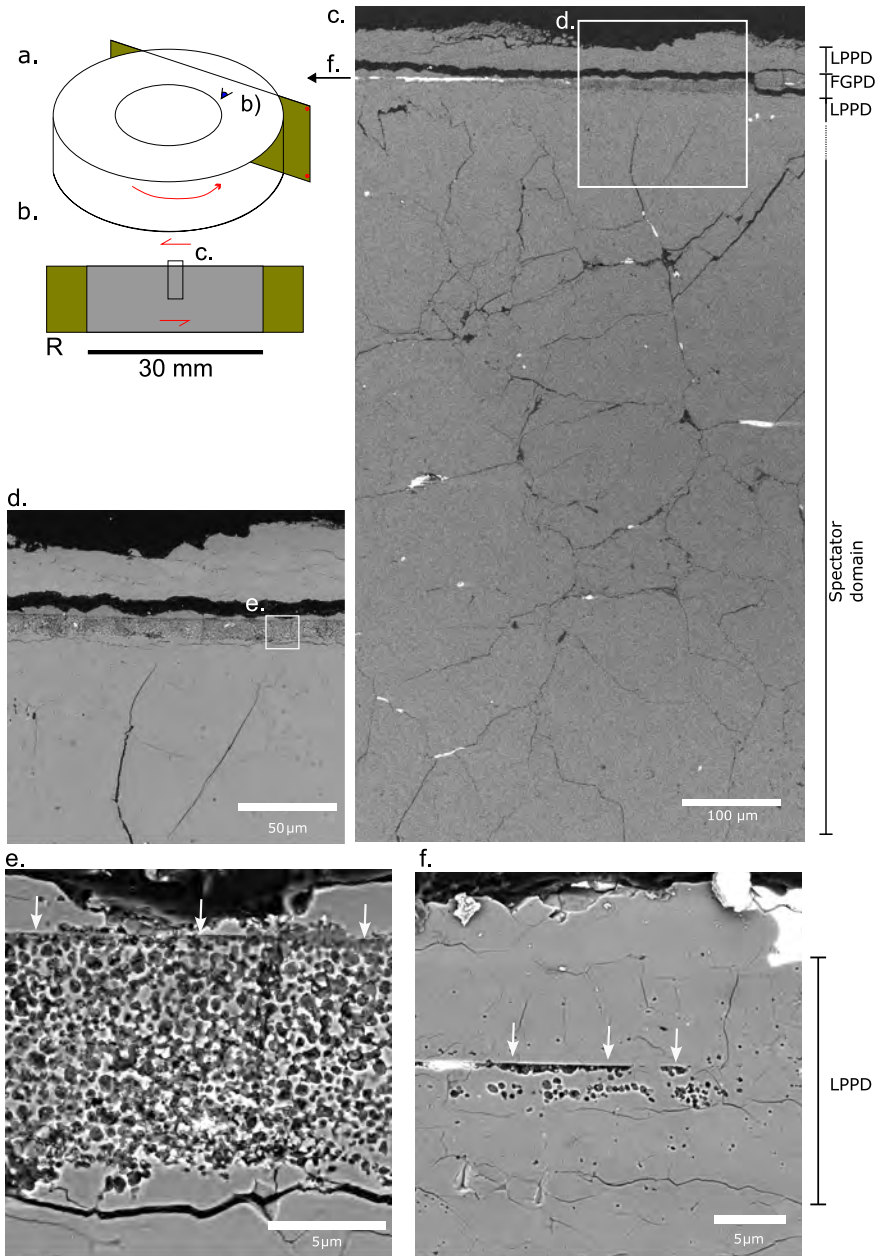

Figure 6. Cross sections of the bare-rock surface sample recovered after the experiment s2007, performed at 20 MPa normal stress with one seismic slip-rate pulse (SEM-BSE images). Sketches of: (a) the sample and (b) the analyzed section, which was on the rotary sample with slip surface on the top (left lateral slip). (c) Transect acquired across the top part of the sample, where the slip surface was preserved between the rotary sample (bottom) and a fragment of the stationary sample (top). (d) Zoom next to the slip surface. A closer zoom showing: (e) the slip surface (top) and adjacent, to the bottom, fine-grained polygonal domain and Low porosity polygonal domain (LPPD); (f) moving to the left of (e), the slip surface was locally welded and surrounded by a LPPD.

for the first slip-rate pulse, becoming smaller during the application of subsequent slip-rate pulses. Instead, σ_n does not affect in a clear way none of the friction coefficients and D_c, while it decreases the slip necessary to reach peak stress during the initial strengthening stage (D_a) ((Smith et al., 2015), see Figure S3 in Supporting Information S1).

Since μ_{peak} increases with application of repeated slip-rate pulses for the gouge layer, it is worth to investigate two parameters in which the peak stress is fundamental: the strength excess ($\tau_{peak} - \tau_0$), where τ_0 is the initial stress and

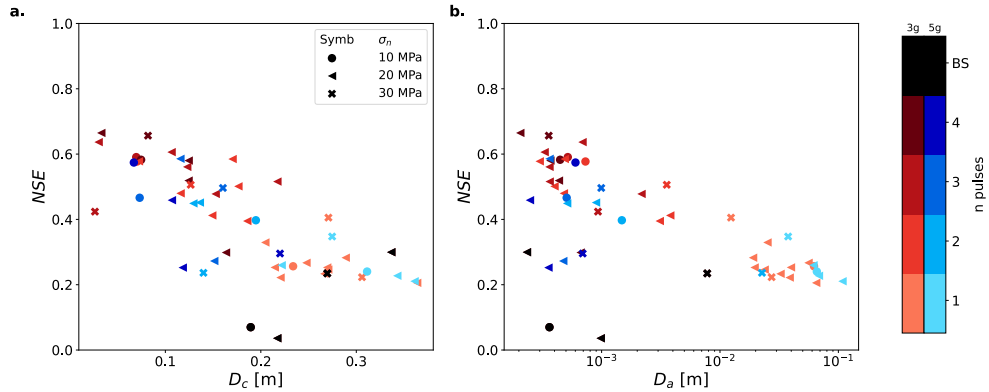

Figure 7. Strength excess parameter S versus (a) slip weakening distance D_c and (b) slip to the onset of dynamic weakening D_a.

the breakdown stress drop (defined as $\Delta\tau_b = \tau_{peak} - \tau_{ss}$). The strength excess and the breakdown stress drop are invoked to determine the spatial re-distribution of stress during earthquake sequences (Cocco et al., 2016; Dalguer et al., 2002). These two parameters are used in the literature to define the parameter $S = (\tau_{peak} - \tau_0)/(\Delta\tau_b)$ (Andrews, 1976; Boatwright & Quin, 1986; Das & Aki, 1977), which is extensively used for modeling the dynamic rupture propagation (Gabriel et al., 2012). Here, we use a slightly different definition of the strength excess more suitable to the interpretation of laboratory results, namely the Normalized Strength Excess (*NSE*) here defined as the ratio between the strength excess and the normal stress σ_n:

$$NSE = \frac{\tau_p - \tau_0}{\sigma_n}$$

To compute the *NSE* for our experiments, we assume $\tau_0 = \tau_{yield}$, where τ_{yield} is the shear stress at the end of the initial (linear) elastic deformation phase ($\tau_{yield} = \mu_0\,\sigma_n$), where μ_0 is the static friction coefficient (i.e., the friction value when slip initiates). It is important to remark that our measure of *NSE* should be considered as a minimum possible value for this parameter, because of our assumption of considering τ_0 equal to the yield stress (beginning of inelastic yielding of the sample) since τ_0 can take any value between the 0 stress and the yield stress.

Among all experiments, *NSE* is the lowest for bare-rock surfaces (0.16 ± 0.12) and the highest for gouge layer experiments at the last applied slip-rate pulse (Figure S4a in Supporting Information S1 and Figure 7). Indeed, *NSE* increases with the number of applied slip-rate pulses from 0.26 ± 0.05 to 0.49 ± 0.15 (Figure 7a and Figure S4a in Supporting Information S1). The breakdown stress drop shows a larger variability with the application of subsequent slip pulses than the peak stress and a more evident dependency on normal stress not observed for *NSE* (Figure S4b in Supporting Information S1). Since *NSE* increases with the number of slip-rate pulses, being larger for gouge than bare-rock experiments, we can assert that *NSE* is a function of the gouge evolution history.

In the slip weakening constitutive model used for modeling dynamic earthquake ruptures (Andrews, 1976), the increase of shear stress from the initial stress τ_0 to τ_{peak} is assumed to occur with zero slip (Ida, 1972) due to the assumption of an elastic and reversible process. In all our experiments, the increase of shear stress from the yield τ_{yield} to the peak stress τ_{peak} occurs over a finite slip D_a (Ohnaka et al., 1997; Ohnaka & Yamashita, 1989). We observe that for gouge layer experiments the *NSE* parameter increases with the number of applied slip-rate pulses while D_a decreases (Figure 7b). In other words, *NSE* decreases for increasing D_a and D_c (Figure 7). This has implications on the energy dissipation during dynamic sliding, as we will discuss in the following.

Globally, the application of subsequent slip-rate pulses leads to a simultaneous increase of μ_{peak} and *NSE*, and a decrease of D_c and D_a, while breakdown stress drop does not show an evident increase. This suggests that, when numerically simulating dynamic ruptures, the employed friction laws should account for: (a) the variability of D_a and D_c (with implications on the energy dissipated during dynamic weakening) and (b) the slip history of fault zone gouge. The slip D_a and the increase of shear stress between 0 and D_a should be considered and included in the dissipated energy. Moreover, a mature fault undergoing a complex history of slip episodes might need a different set of mechanical parameters (*NSE*, D_c, D_a) with respect to an immature fault.

4.2. Microstructural Evolution of the Sheared Gouge Layer With Slip-Rate Pulses

In previous studies performed with rotary shear apparatuses, the mechanical data were coupled with post-mortem microstructural analysis of the calcite gouge layers to determine the deformation mechanisms activated in the experiments (De Paola et al., 2011, 2015; Demurtas et al., 2019, 2021; Pozzi et al., 2018; Rempe et al., 2013, 2017, 2020; Smith et al., 2013, 2015). In single slip-rate pulse experiments performed at a $\sigma_n = 25$ MPa, slip rate of 1.4 m/s for 0.045 m, 0.07 m or 1 m of slip, microstructural domains similar to those found in our experiments developed during strain localization (Pozzi et al., 2018). At the onset of slip (0.045 m < D_a), the spectator domain was found to be comminuted into a cataclastic domain crosscut by R-type shear fractures which in our case are not recognized (Pozzi et al., 2018). Then, with increasing slip (0.07 m < D_a) a PSZ developed which, with further slip (0.9 m > D_c > D_a), evolved into a fully recrystallized 25–30 μm thick PSZ similar to the FGPD found in our experiments. For instance, in Pozzi et al. (2018) the PSZ had a polygonal texture with triple junctions, grain size <1 μm and was separated by sharp and continuous mirror-like surfaces (Mirror Surface (MS)) from the bounding sintered zone with grain size >1 μm. The MSs were suggested to develop during the deceleration stage of the slip-rate pulse and interpreted to mark a rheological transition, that is, the impossibility during the deceleration stage for the PSZ to adjust to decreasing strain rate by increasing its thickness, due to the larger grain size of the adjacent sintered domains (Pozzi et al., 2018). Similar microstructures were found in calcite gouge layers sheared at a $\sigma_n = 8.5$ MPa and slip rate of 1 m/s for 0.01 m, 0.13 m, 0.43 m and 1.3 m of slip (Rempe et al., 2017). In this case, the process of strain localization was also evidenced thanks to the insertion of a strain marker made of dolomite gouge (Rempe et al., 2017). Similarly, PSZs with nanoparticles, polygonal textures, clasts with pores due to decarbonation, bordered by sintered domains were found in experiments performed at similar loading conditions (σ_n = 8.5–17.5 MPa, slip rate of 1.0–1.3 m/s and 0.3–0.4 m of slip under room humidity conditions) (Demurtas et al., 2021; Smith et al., 2015). The microstructures found in our experiments after one slip-rate pulse are consistent with the above findings: the FGPDs and LPPDs are similar, respectively, to the PSZs and sintered domains described in previous studies. Moreover, the LPPD has non-uniform grain size, spanning from <1 μm to <40 μm, and the grains have, locally, irregular and sharp grain boundaries (Figures 5c and 5d). The (a) large range of grain size and shape (from relatively irregular to euhedral) of the grains, (b) the presence of complete and incomplete triple junctions and, (c) the occurrence of partly decomposed dolomite grains (decarbonation temperature >550°C, Figure 5c (Rodriguez-Navarro et al., 2012);), are consistent with the interpretation that LPPD is the result of high temperature (static) sintering (or annealing) of the comminuted domain. This interpretation suggests that most of the shear strain is localized in the FGPDs (or PSZ), where frictional heat is generated and then diffused into the gouge layer.

With progressing slip-rate pulses, the mechanical behavior of the simulated fault is affected by the strain localization process in the gouge layer and, vice-versa, strain localization process appears to be influenced by the previous slip-rate pulses and their associated thermal pulses. In the following section, we interpret our microstructural observations for gouge layer experiments (Figures 4 and 5) by means of a simplified sketch (Figure 7). In the first slip-rate pulse (Figure 8c), the PSZ-1 (1 stands for first pulse) and the associated sintered (or LPPD) domain are localized next to the stationary side (Figure 4c). The PSZ-1 locally includes nanoparticle pods with nanopores and Y-shears, which are systematically found in the four slip-rate pulse experiments and is bordered by R-type fractures below it (i.e., toward the rotary side). After the second slip-rate pulse (Figure 8d), a PSZ-2 appears (Figure 4d). We speculate that PSZ-2 localized at the weak interface between the (sintered) LPPD (quite cohesive) and the comminuted domain (poorly cohesive). In the third slip-rate pulse (Figure 8e), the PSZ-3 possibly overprinted one of the previous PSZs (Figure 4e). After the first three slip-rate pulses, the PSZs are localized at 100–300 μm from the contact with the stationary side, forced by the experimental setup (Rempe et al., 2017). The thermal heat pulses associated with the second and third slip-rate pulse resulted in annealing (or hot sintering) of the previous PSZs and their respective comminuted domain and LPPDs. Sintering processes drove to a gradual increase of grain size across the gouge layer and the overall sintered zone was about 500–600 μm thick (Figure 4e). In the fourth slip-rate pulse (Figure 7f), a new PSZ-4 developed at ca 500–600 μm from the contact with the stationary side and located at the boundary between the LPPD and the comminuted domain (Figures 4e and 4f). Remarkably, PSZ-4 includes a characteristic fabric with sharp and continuous fracture parallel to the slip direction, filled with nanoparticles crosscut by sharp surface interpreted as Y-shears (Figures 5g and 5h). The R-shears fractures formed next to the previous PSZs 1-2-3 were healed after the fourth slip-rate pulse and fragments of previous PSZs were folded and plastically deformed (Figure 5f). The PSZ-4 was surrounded by its sintered zone developed during frictional heat diffusing away, similarly as the previous PSZs. In this case,

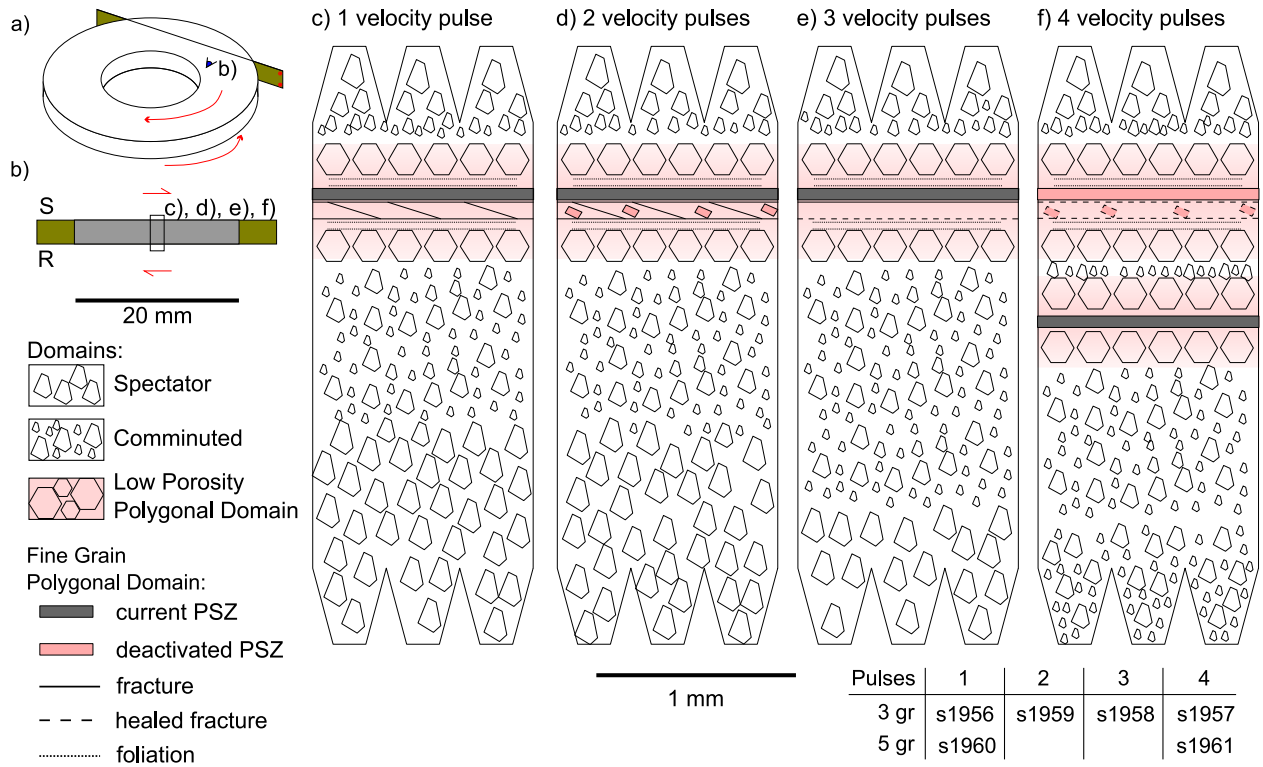

Figure 8. Schematic illustration of the microstructural evolution of the gouge layer with the number of deformation pulses. (a) sketch of the sample, (b) sketch of the analyzed sections, (c) one slip-rate pulse deformation, (d) two deformation slip-rate pulses, (e) three deformation slip-rate pulses, (f) four deformation slip-rate pulses. We report the identified domains and the interpretation of the fine grain polygonal domain (Fine-grained polygonal domain) as principal slip zones|principal slipping zone and their evolution through the four slip-rate pulses.

about half of the gouge layer thickness was overprinted by the sintered domains at the end of the fourth slip-rate pulse experiments (ca. 750–800 μm) (Figure 4f).

We suggest that the shift of strain localization from the area where PSZ-1, 2, and 3 developed to the area where PSZ-4 developed was caused by the increase of thickness of the sintered domain with respect to the total thickness of the gouge layer, due to the three previous slip-rate pulses. The increase of sintered layer thickness might represent a process of healing and therefore bulk hardening of the gouge layer. Upon a fourth slip-rate pulse, the fact that the upper part of gouge layer was sintered and had a higher strength might force localization next to or at the boundary between the sintered zone and the comminuted layer. The overall increase of the thickness of LPPD might reflect the increase of μ_{peak}, and promote the lowest values of D_a and D_c attributed to the newly formed PSZ-4.

Previous works highlighted that multiple PSSs or MSs can develop even during gouge experiments with only one slip-rate pulse (Rempe et al., 2014). However, we point out that PSSs or MSs are different than the PSZs discussed here: in fact, PSZs have a clear finite thickness and peculiar grain size (<1 μm), which is clearly lower than the one in the surrounding sintered domains (<5–10 μm), whereas the PSSs or MSs are thin discontinuities/planar features that eventually overprint the PSZs or the PSZ-sintered domain boundary (Figures 5e and 5f). Multiple PSSs or MSs can form due to sample edge effects, for example, approaching to the external radius of the gouge layer (Rempe et al., 2014), or due to the interaction of the sample holder roughness with the gouge layer (Figure S5 in Supporting Information S1). We do not exclude that PSSs or MSs can form during the deceleration stage of each event and represent a brittle overprint over the PSZ active during the event (Pozzi et al., 2018). Here we also report the presence of PSSs formed in any of the first three slip-rate pulses that appear as welded at the end of the fourth slip-rate pulse (Figure 5f).

In our experiments, there are microstructural features pointing to the occurrence of high temperatures within the slip zone: the sintered, statically recrystallized domains surrounding the PSZs that included partially decomposed

dolomite grains (Figures 5c and 5d) and the nanogranular PSZs themselves. In fact, together with sintering there are two physical processes that might occur in the PSZ or nearby it. First, the activation of viscous creep processes (Ashby & Verrall, 1973; De Paola et al., 2015; Pozzi et al., 2018, 2019), which is evidenced by the presence of euhedral calcite grains with triple junctions in our PSZs-4. Moreover, recent microstructural with EBSD showed the activation of grain size sensitive and grain size insensitive flow indicative of high temperature and strain rate viscous creep (Demurtas et al., 2019; Pozzi et al., 2019). Second, the activation of thermal decomposition (Han et al., 2007, 2010) by decarbonation of dolomite clasts (Figure 5c), and locally by decarbonation of calcite in the PSZ-4 (gouge, Figure 5h) or right below the slip surface (bare-rock, Figure 6e). The decarbonation of calcite appears with a peculiar texture suggesting the reaction of lime (the product of calcite decarbonation reaction) with air humidity to produce portlandite (Figures 5h and 6e).

4.3. Evolution of Mechanical Energy

The main outcome of the mechanical and microstructural investigations is the evidence that the gouge layer evolved with the application of repeated slip-rate pulses. Here we discuss if the evolution of the gouge layer influences the work dissipated during the simulated dynamic instabilities.

We can analyze the retrieved values of breakdown work Wb (Cocco et al., 2006, 2023; Tinti et al., 2005) (Figure 9a) by integrating the evolution of shear stress with slip

$$Wb = \int_0^{D_c} [\tau(u) - \tau_{ss}]\, du,$$

We distinguish two contributions to Wb (Figure 9a), following (Ohnaka, 2003): the energy dissipated from the start of sliding to the beginning of dynamic weakening (Wb_A), which is the energy dissipated during the strengthening stage characterized by the stress evolution from τ_0 to the τ_{peak} over D_a (Figure 9a)

$$Wb_A = \int_0^{D_a} [\tau(u) - \tau_{ss}]\ du$$

and the energy dissipated during the weakening stage, from D_a to D_c (Figure 8d2)

$$Wb_B = \int_{D_a}^{D_c} [\tau(u) - \tau_{ss}]\ du$$

The values inferred for Wb decreased with the application of repeated slip-rate pulses in gouge layer experiments (1.21 ± 0.42 MJ/m^2 in the first slip pulse and 0.34 ± 0.31 MJ/m^2 in the fourth pulse), with the value obtained at the application of the fourth pulse being similar to that inferred for bare-rock surface experiments (0.43 ± 0.24 MJ/m^2) (Figure 9b). Indeed, Wb_A drastically decreased after the first slip-rate pulse (0.55 ± 0.23 MJ/m^2), and remained constant for the other slip-rate pulses: 0.012 ± 0.02, 0.005 ± 0.005, and 0.004 ± 0.007 MJ/m^2, for the second, third and fourth slip-rate pulse, respectively (Figure 9c). This is coherent with the retrieved D_a values, which strongly decrease with the application of the subsequent slip-rate pulses. Ohnaka (2013) interpreted Wb_A as the energy spent to create microcracks and crack-coalescence in intact rocks, and for asperity interlocking and asperity plowing in bare rocks. We can interpret Wb_A as the energy dissipated to organize the gouge layer during initial strain localization. After the first slip-rate pulse, the layer was already organized (and strain localized) and the onset of the weakening stage required lower amount of energy (Figure 9b) and lower value of D_a (Figure 7b). Wb_B was the energy dissipated during the dynamic weakening stage and it slightly decreased during the subsequent slip-rate pulses: 0.57 ± 0.24, 0.50 ± 0.35, 0.41 ± 0.36, and 0.34 ± 0.31 MJ/m^2, for the first, second, third and fourth slip-rate pulse, respectively (Figure 9d). The energy dissipated during the dynamic weakening stage for bare-rock surface has similar values. For bare rock experiments, Wb_A and Wb_B had values similar to those of the fourth slip-rate pulse in gouge layer (0.03 ± 0.03 MJ/m^2 and 0.43 ± 0.24 MJ/m^2, respectively). Ohnaka (2013) underlined that the preparatory phase of inelastic deformation is an integral part of the eventual macroscopic shear faulting and the associated stress drop.

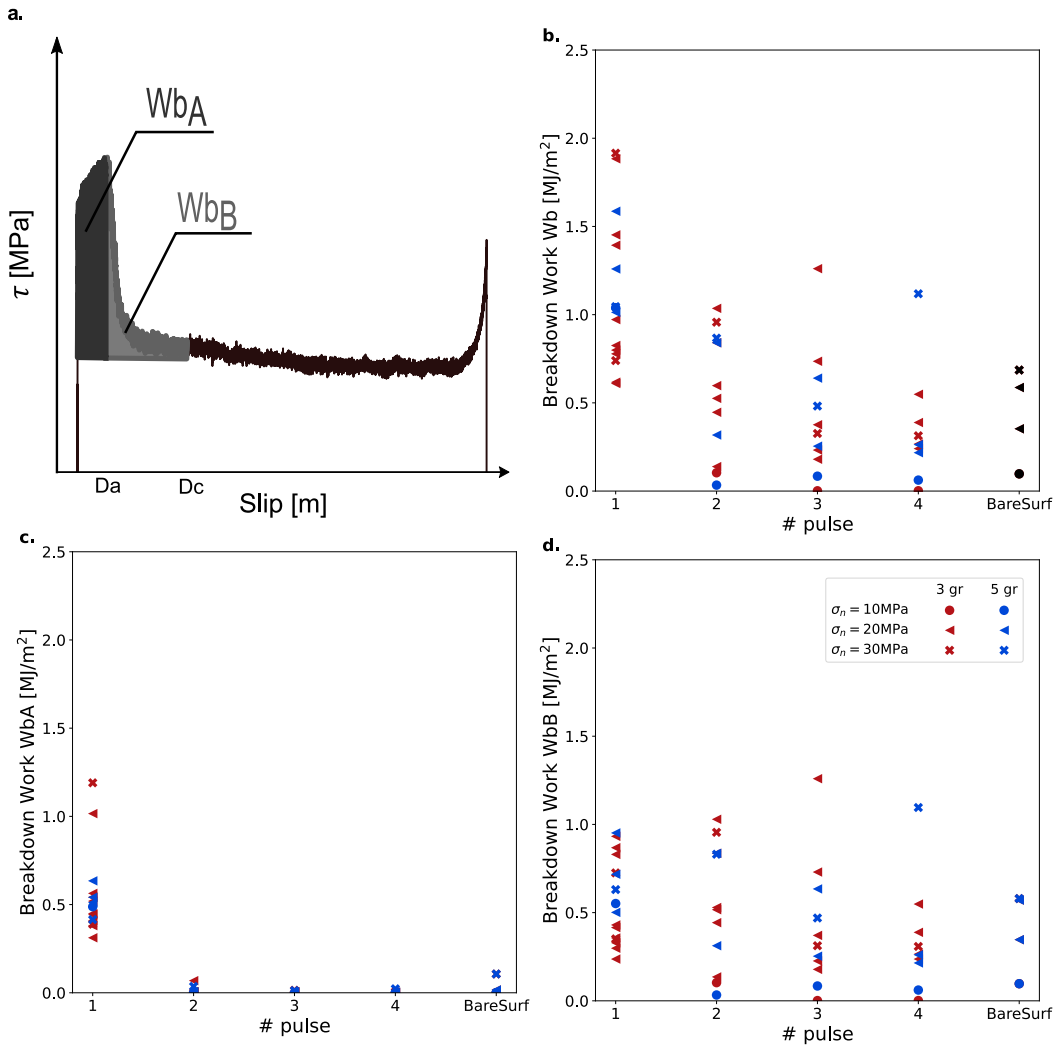

Figure 9. Breakdown work evolution with the number of slip-rate pulses for gouge layer experiments and bare-rock surface experiments (a) Sketch for the definition of the partition on the breakdown work Wb_A and Wb_B; (b) Breakdown work (sum of Wb_A and Wb_B) vs. the number of the slip-rate pulse and comparison with bare rock experiments (c) breakdown work Wb_A dissipated to reach the slip distance D_a and (d) breakdown work Wb_B dissipated from D_a to reach the slip weakening distance D_c.

The importance of Wb_A, has also been investigated in modeling the seismic cycle (Bolotskaya & Hager, 2022), where it has been showed how an initial inelastic deformation produced an oscillatory phase in a 1D spring slider model. We experimentally quantified Wb_A and we observed that its contribution may be significant (45% of Wb) at the early stage of slip of a not-localized gouge layer.

Finally, we also estimated the energy dissipated in the direction perpendicular to the experimental fault (i.e., the normal work *NW*), for both gouge layer and bare-rock surface experiments:

$$NW = \int_0^{t(D_c)} \sigma_n(t)\, \dot{\delta}(t)\, dt$$

Where $\dot{\delta}$ is shortening rate and $t(D_c)$ is the time at which slip is equal to D_c. Since $\sigma_n(t)$ is almost constant during the experiment, the trend of *NW* with slip was following the one of the layer's shortening (Figure S6 in Supporting Information S1). We considered a positive value of *NW* for the energy dissipated due to compaction and negative value for the one due to dilation (Figure 10). *NW* was six orders of magnitude lower than *Wb*. *NW* decreased with

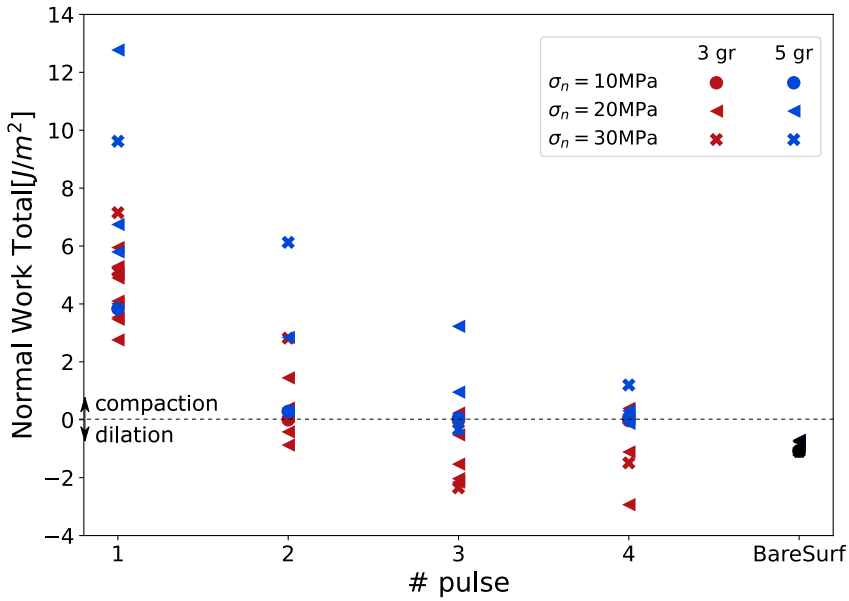

Figure 10. Energy dissipated normal to the fault (normal work, *NW*), due to compaction/dilation of the gouge layer.

the increase of the number of slip-rate pulses from ca. 5.6 ± 1.7 J/m^2 at the first slip pulse to ca. -0.2 ± 0.9 J/m^2 at the forth slip pulse and -0.7 ± 0.4 J/m^2 in bare-rock surface experiments.

The evolution of dilatancy was the only visible difference between thinner (3 g of gouge) and thicker (5 g of gouge) gouge layers (Figure 10). The thicker gouge layers, compared to the thinner gouge layer, had overall lower μ_{peak} for the same slip-rate pulse number (Figure 3b) and achieved dilatant behavior at larger number of slip-rate pulses than the thinner gouge layers (Figure 10). This might happen because the sintered gouge layer thickness over the total gouge layer thickness was lower in thicker gouge layers, therefore sintering and healing of the entire gouge layer requires larger number of slip-rate pulses.

5. Conclusions

We applied multiple slip-rate pulses to an experimental fault consisting of a gouge layer obtained from calcite-bearing rocks. Experiments were conducted at $\sigma_n = 10$, 20, and 30 MPa on a thinner and a thicker gouge layer. We also performed experiments with bare-rock surfaces of calcite-bearing rocks. Friction coefficients (μ_0, μ_{peak}, μ_{ss}, μ_{rest}), characteristic slip distances (D_c, D_a) and the dissipated energy (*Wb*, *NW*) were compared between the two end-members (fault gouge—bare-rock) and considering the number of applied slip-rate pulses, σ_n, and initial thickness (for fault gouge). We have largely extended the analyses of Smith et al. (2015) by applying four consecutive slip-rate pulses, by comparing fault gouge with bare-rock surfaces, by extending the microanalyses of gouge samples and bare-rock surface sample and by measuring dissipated energy.

Our results show that the initial friction and the steady-state friction level are nearly constant during the application of repeated slip-rate pulses and systematically higher to values inferred for bare-rock surface. Differently, peak friction increases with the application of subsequent slip-rate pulses, being higher than the ones measured in bare-rock surfaces. The increase of peak shear stress yields an increase of the *NSE* parameter with the application of subsequent slip-rate pulses, but not an increase of energy dissipation (breakdown work *Wb*) because the associated slip values, D_c and D_a, decreases with the application of subsequent slip-rate pulses.

We have analyzed the energy dissipation in the experimental fault by computing the breakdown work, and its partitioning (Wb_A and Wb_B) during the consecutive dynamic strengthening and weakening stages of friction evolution. Surprisingly, the dissipated energy is nearly the same during each applied slip-rate pulse and bare surface experiments. Only breakdown work computed after the application of one slip-rate pulse (*Wb* and Wb_A in Figures 9b and 9c) are relatively higher, because of the larger value of D_a.

The microstructural analysis shows the localization of strain in a PSZ with nanometric grain size, surrounded by low porosity sintered domains in each slip-rate pulse, with subsequent overprint of the structures generated during the application of the previous slip-rate pulses. Moreover, strain localization position shifts between PSZ-1, PSZ-2, PSZ-3 and PSZ-4 and thickness of sintered gouge domain increases with increasing number of applied slip-rate pulses.

By interpreting results from microstructural analysis together with the measures of breakdown work, we show that the PSZ during repeated slip-rate pulses migrates within the gouge layer. This means that the strain localization process identifies the PSZ trying to minimize energy dissipation within the experimental fault zone to values similar to those of bare-rock surfaces, which can be considered as the end member of strain localization. The thinner fault (3 g of gouge) seems to promote strain localization than the thicker fault. We suggest that the same processes can occur during repeated dynamic instabilities on natural fault zones, providing a mechanism for creating multiple PSZs within the FC while keeping energy dissipation nearly constant.

We have computed the energy dissipated perpendicularly to the slip direction (*NW*). We show that it is six orders of magnitude smaller than breakdown work and it decreases with the application of repeated slip-rate pulses approaching the values inferred for bare-rock surface. The thinner fault (3 g) has lower *NW* values than the thicker fault (5 g), also involving dilation.

Our conclusions are valid for calcite-bearing fault rocks. More experiments on different rocks are necessary to generalize these results to the mechanics of earthquakes and faulting.

Data Availability Statement

All raw experimental data are available at Cornelio C, (2023).

Acknowledgments
This study has received funding from the European Research Council (ERC) under the European Union's Horizon 2020 research and innovation programme (Grant agreement 856559). MC participated in this work as Principal Investigator of the ERC project FEAR (Grant agreement 856559) under the European Community's Horizon 2020 Framework Programme. SA, CC, and ES participated in this work in the framework of the ERC project FEAR (Grant agreement 856559) under the European Community's Horizon 2020 Framework Programme. This work was also supported by Project FSE+ 2021–2027, Contributi premiali per i ricercatori e assegnisti di ricerca per rafforzarne la condizione professionale e potenziare il sistema della ricerca del Lazio (Atto n. G05411 del 05/05/2022) attributed to SA, ES and CC. GDT acknowledges the ERC CoG project 614705 NOFEAR and Progetto PRIN 2022 Di Toro - 2022WE2JY9. CC acknowledges Christopher Harbord for the technical development of the gouge sample holder, Stefano Castelli for the optical scans of the polished samples, and Giacomo Pozzi and Manuela Nazzari for assistance with the FEG-SEM at INGV, and Jacopo Nava and Leonardo Tauro for assistance with the FEG-SEM at University of Padua. Open access publishing facilitated by Istituto Nazionale di Geofisica e Vulcanologia, as part of the Wiley - CRUI-CARE agreement.

References

Amato, A., Azzara, R., Chiarabba, C., Cimini, G. B., Cocco, M., Di Bona, M., et al. (1998). The 1997 Umbria-Marche, Italy, earthquake sequence: A first look at the main shocks and aftershocks. *Geophysical Research Letters*, *25*(15), 2861–2864. https://doi.org/10.1029/98GL51842

Andrews, D. J. (1976). Rupture velocity of plane strain shear cracks. *Journal of Geophysical Research*, *81*(32), 5679–5687. https://doi.org/10.1029/JB081i032p05679

Archard, J. F. (1959). The temperature of rubbing surfaces. *Wear*, *2*(6), 438–455. https://doi.org/10.1016/0043-1648(59)90159-0

Aretusini, S., Meneghini, F., Spagnuolo, E., Harbord, C., & Di Toro, G. (2021). Fluid pressurisation and earthquake propagation in the Hikurangi subduction zone. *Nature Communications*, *12*(1), 2481. https://doi.org/10.1038/s41467-021-22805-w

Aretusini, S., Mittempergher, S., Plümper, O., Spagnuolo, E., Gualtieri, A. F., & Di Toro, G. (2017). Production of nanoparticles during experimental deformation of smectite and implications for seismic slip. *Earth and Planetary Science Letters*, *463*, 221–231. https://doi.org/10.1016/j.epsl.2017.01.048

Ashby, M. F., & Verrall, R. A. (1973). Diffusion-accommodated flow and superplasticity. *Acta Metallurgica*, *21*(2), 149–163. https://doi.org/10.1016/0001-6160(73)90057-6

Bedford, J. D., Hirose, T., & Hamada, Y. (2023). Rapid Fault healing after seismic slip. *Journal of Geophysical Research: Solid Earth*, *128*(6), e2023JB026706. https://doi.org/10.1029/2023JB026706

Beeler, N. M., & Tullis, T. E. (1997). The roles of time and displacement in velocity-dependent volumetric strain of fault zones. *Journal of Geophysical Research*, *102*(B10), 22595–22609. https://doi.org/10.1029/97jb01828

Ben-Menahem, A. (1991). Four thousand years of seismicity along the dead sea rift. *Journal of Geophysical Research*, *96*(B12), 20195–20216. https://doi.org/10.1029/91JB01936

Boatwright, J., & Quin, H. (1986). The seismic radiation from a 3-D dynamic model of a complex rupture process. Part I: Confined ruptures. In *Earthquake source mechanics* (pp. 97–109). https://doi.org/10.1029/GM037p0097

Bolotskaya, E., & Hager, B. H. (2022). A 1D spring-slider model with a simple poly-linear failure law produces rich variations in slip behavior. *Bulletin of the Seismological Society of America*, *112*(6), 2795–2811. https://doi.org/10.1785/0120220052

Boneh, Y., Chang, J. C., Lockner, D. A., & Reches, Z. (2014). Evolution of wear and friction along experimental faults. *Pure and Applied Geophysics*, *171*(11), 3125–3141. https://doi.org/10.1007/s00024-014-0801-3

Boneh, Y., & Reches, Z. (2018). Geotribology - friction, wear, and lubrication of faults. *Tectonophysics*, *733*, 171–181. https://doi.org/10.1016/j.tecto.2017.11.022

Boneh, Y., Sagy, A., & Reches, Z. (2013). Frictional strength and wear-rate of carbonate faults during high-velocity, steady-state sliding. *Earth and Planetary Science Letters*, *381*, 127–137. https://doi.org/10.1016/j.epsl.2013.08.050

Brantut, N., Schubnel, A., Rouzaud, J.-N., Brunet, F., & Shimamoto, T. (2008). High-velocity frictional properties of a clay-bearing fault gouge and implications for earthquake mechanics. *Journal of Geophysical Research*, *113*(B10), B10401. https://doi.org/10.1029/2007JB005551

Brantut, N., & Viesca, R. C. (2017). The fracture energy of ruptures driven by flash heating. *Geophysical Research Letters*, *44*(13), 6718–6725. https://doi.org/10.1002/2017GL074110

Byerlee, J. (1978). Friction of rocks. *Pure and Applied Geophysics PAGEOPH*, *116*(4–5), 615–626. https://doi.org/10.1007/BF00876528

Caine, J. S., Evans, J. P., & Forster, C. B. (1996). Fault zone architecture and permeability structure. *Geology*, *24*(11), 1025. https://doi.org/10.1130/0091-7613(1996)024<1025:FZAAPS>2.3.CO;2

Carslaw, H. S., & Jaeger, J. C. (1959). *Conduction of heat in solids (Secend EDI)*. Oxford University Press.

Chen, J., Verberne, B. A., & Spiers, C. J. (2015). Effects of healing on the seismogenic potential of carbonate fault rocks: Experiments on samples from the Longmenshan Fault, Sichuan, China. *Journal of Geophysical Research: Solid Earth*, *120*(8), 5479–5506. https://doi.org/10.1002/2015JB012051

Chester, F. M., & Chester, J. S. (1998). Ultracataclasite structure and friction processes of the Punchbowl fault, San Andreas system, California. *Tectonophysics*, *295*(1), 199–221. https://doi.org/10.1016/S0040-1951(98)00121-8

Chester, F. M., & Logan, J. M. (1986). Implications for mechanical properties of brittle faults from observations of the Punchbowl fault zone, California. *Pure and Applied Geophysics*, *124*(1), 79–106. https://doi.org/10.1007/BF00875720

Chiaraluce, L., Valoroso, L., Piccinini, D., Di Stefano, R., & De Gori, P. (2011). The anatomy of the 2009 L'Aquila normal fault system (central Italy) imaged by high resolution foreshock and aftershock locations. *Journal of Geophysical Research*, *116*(B12), B12311. https://doi.org/10.1029/2011JB008352

Chinello, M., Bersan, E., Fondriest, M., Tesei, T., Gomila, R., & Di Toro, G. (2023). Seismic cycle in bituminous dolostones (Monte CAMICIA thrust zone, central Apennines, Italy). *Geochemistry, Geophysics, Geosystems*, *24*(12), e2023GC011063. https://doi.org/10.1029/2023GC011063

Cocco, M., Aretusini, S., Cornelio, C., Nielsen, S. B., Spagnuolo, E., Tinti, E., & Di Toro, G. (2023). Fracture energy and breakdown work during earthquakes. *Annual Review of Earth and Planetary Sciences*, *51*(1), 217–252. https://doi.org/10.1146/annurev-earth-071822-100304

Cocco, M., Spudich, P., & Tinti, E. (2006). On the mechanical work absorbed on faults during earthquake ruptures. In *Agu monograph: Earthquakes: Radiated energy and the physics of faulting* (pp. 237–254). https://doi.org/10.1029/170GM24

Cocco, M., Tinti, E., & Cirella, A. (2016). On the scale dependence of earthquake stress drop. *Journal of Seismology*, *20*(4), 1151–1170. https://doi.org/10.1007/s10950-016-9594-4

Collettini, C., Di Stefano, G., Carpenter, B., Scarlato, P., Tesei, T., Mollo, S., et al. (2014). A novel and versatile apparatus for brittle rock deformation. *International Journal of Rock Mechanics and Mining Sciences*, *66*, 114–123. https://doi.org/10.1016/j.ijrmms.2013.12.005

Collettini, C., Tesei, T., Scuderi, M. M., Carpenter, B. M., & Viti, C. (2019). Beyond Byerlee friction, weak faults and implications for slip behavior. *Earth and Planetary Science Letters*, *519*, 245–263. https://doi.org/10.1016/j.epsl.2019.05.011

Cornelio, C. (2023). Mechanical data for the manuscript: Multiple seismic slip-rate pulses and mechanical and textural evolution of calcite-bearing fault gouges [Dataset]. *Zenodo*. https://doi.org/10.5281/zenodo.8420134

Cornelio, C., Spagnuolo, E., Aretusini, S., Nielsen, S., Passelègue, F., Violay, M., et al. (2022). Determination of parameters characteristic of dynamic weakening mechanisms during seismic faulting in cohesive rocks. *Journal of Geophysical Research: Solid Earth*, *127*, (7), e2022JB024356. https://doi.org/10.1029/2022JB024356

Dalguer, L. A., Irikura, K., Zhang, W., & Riera, J. D. (2002). Distribution of dynamic and static stress changes during 2000 tottori (Japan) earthquake: Brief interpretation of the earthquake sequences; foreshocks, mainshock and aftershocks. *Geophysical Research Letters*, *29*(16), 4–5. https://doi.org/10.1029/2001GL014333

Das, S., & Aki, K. (1977). Fault plane with barriers: A versatile earthquake model. *Journal of Geophysical Research*, *82*(36), 5658–5670. https://doi.org/10.1029/JB082i036p05658

Demurtas, M., Fondriest, M., Balsamo, F., Clemenzi, L., Storti, F., Bistacchi, A., & Di Toro, G. (2016). Structure of a normal seismogenic fault zone in carbonates: The Vado di Corno Fault, Campo Imperatore, Central Apennines (Italy). *Journal of Structural Geology*, *90*, 185–206. https://doi.org/10.1016/j.jsg.2016.08.004

Demurtas, M., Smith, S. A. F., Prior, D. J., Brenker, F. E., & Di Toro, G. (2019). Grain size sensitive creep during simulated seismic slip in nanogranular fault gouges: Constraints from transmission kikuchi diffraction (TKD). *Journal of Geophysical Research: Solid Earth*, *124*(10), 10197–10209. https://doi.org/10.1029/2019JB018071

Demurtas, M., Smith, S. A. F., Spagnuolo, E., & Di Toro, G. (2021). Frictional properties and microstructural evolution of dry and wet calcite–dolomite gouges. *Solid Earth*, *12*(3), 595–612. https://doi.org/10.5194/se-12-595-2021

De Paola, N., Hirose, T., Mitchell, T., Di Toro, G., Viti, C., & Shimamoto, T. (2011). Fault lubrication and earthquake propagation in thermally unstable rocks. *Geology*, *39*(1), 35–38. https://doi.org/10.1130/G31398.1

De Paola, N., Holdsworth, R. E., Viti, C., Collettini, C., & Bullock, R. (2015). Can grain size sensitive flow lubricate faults during the initial stages of earthquake propagation? *Earth and Planetary Science Letters*, *431*, 48–58. https://doi.org/10.1016/j.epsl.2015.09.002

Dieterich, J. H. (1972). Time-dependent friction in rocks. *Journal of Geophysical Research*, *77*(20), 3690–3697. https://doi.org/10.1029/jb077i020p03690

Dieterich, J. H. (1981). Constitutive properties of faults with simulated gouge. In *Mechanical behavior of crustal rocks* (pp. 103–120). https://doi.org/10.1029/GM024p0103

Di Toro, G., Han, R., Hirose, T., De Paola, N., Nielsen, S., Mizoguchi, K., et al. (2011). Fault lubrication during earthquakes. *Nature*, *471*(7339), 494–498. https://doi.org/10.1038/nature09838

Di Toro, G., Niemeijer, A. R., Tripoli, A., Nielsen, S. B., Di Felice, F., Scarlato, P., et al. (2010). *From field geology to earthquake simulation: A new state-of-The-art tool to investigate rock friction during the seismic cycle (SHIVA)*, Springer-Verlag Italia s.r.l. (Vol. 21, pp. 95–114). https://doi.org/10.1007/s12210-010-0097-x

Faulkner, D. R., Jackson, C. A. L., Lunn, R. J., Schlische, R. W., Shipton, Z. K., Wibberley, C. A. J., & Withjack, M. O. (2010). A review of recent developments concerning the structure, mechanics and fluid flow properties of fault zones. *Journal of Structural Geology*, *32*(11), 1557–1575. https://doi.org/10.1016/j.jsg.2010.06.009

Faulkner, D. R., Lewis, A. C., & Rutter, E. H. (2003). On the internal structure and mechanics of large strike-slip fault zones: Field observations of the carboneras fault in southeastern Spain. *Tectonophysics*, *367*(3), 235–251. https://doi.org/10.1016/S0040-1951(03)00134-3

Ferri, F., Di Toro, G., Hirose, T., & Shimamoto, T. (2010). Evidence of thermal pressurization in high-velocity friction experiments on smectite-rich gouges: Thermal pressurization of clay-rich gouges. *Terra Nova*, *22*(5), 347–353. https://doi.org/10.1111/j.1365-3121.2010.00955.x

Fondriest, M., Balsamo, F., Bistacchi, A., Clemenzi, L., Demurtas, M., Storti, F., & Di Toro, G. (2020). Structural Complexity and Mechanics of a Shallow Crustal Seismogenic Source (Vado di Corno Fault Zone, Italy). *Journal of Geophysical Research: Solid Earth*, *125*(9), e2019JB018926. https://doi.org/10.1029/2019JB018926

Fondriest, M., Smith, S. A. F., Candela, T., Nielsen, S. B., Mair, K., & Di Toro, G. (2013). Mirror-like faults and power dissipation during earthquakes. *Geology*, *41*(11), 1175–1178. https://doi.org/10.1130/G34641.1

Gabriel, A.-A., Ampuero, J.-P., Dalguer, L. A., & Mai, P. M. (2012). The transition of dynamic rupture styles in elastic media under velocity-weakening friction. *Journal of Geophysical Research*, *117*(B9). https://doi.org/10.1029/2012JB009468

Goldsby, D. L., & Tullis, T. E. (2011). Flash heating leads to low frictional strength of crustal rocks at earthquake slip rates. *Science*, *334*(6053), 216–218. https://doi.org/10.1126/science.1207902

Han, R., Hirose, T., & Shimamoto, T. (2010). Strong velocity weakening and powder lubrication of simulated carbonate faults at seismic slip rates. *Journal of Geophysical Research*, *115*(B3). https://doi.org/10.1029/2008JB006136

Han, R., Shimamoto, T., Hirose, T., Ree, J.-H., & Ando, J.-i. (2007). Ultralow friction of carbonate faults caused by thermal decomposition. *Science*, *316*(5826), 878–881. https://doi.org/10.1126/science.1139763

Heaton, T. H. (1990). Evidence for and implications of self-healing pulses of slip in earthquake rupture. *Physics of the Earth and Planetary Interiors*, *64*(1), 1–20. https://doi.org/10.1016/0031-9201(90)90002-F

Hirose, T., Mizoguchi, K., & Shimamoto, T. (2012). Wear processes in rocks at slow to high slip rates. *Journal of Structural Geology*, *38*, 102–116. https://doi.org/10.1016/j.jsg.2011.12.007

Ida, Y. (1972). Cohesive force across the tip of a longitudinal-shear crack and Griffith's specific surface energy. *Journal of Geophysical Research*, *77*(20), 3796–3805. https://doi.org/10.1029/JB077i020p03796

Leah, H., Fondriest, M., Lucca, A., Storti, F., Balsamo, F., & Di Toro, G. (2018). Coseismic extension recorded within the damage zone of the Vado di Ferruccio Thrust Fault, Central Apennines, Italy. *Journal of Structural Geology*, *114*, 121–138. https://doi.org/10.1016/j.jsg.2018.06.015

Logan, J. M., Dengo, C. A., Higgs, N. G., & Wang, Z. Z. (1992). Chapter 2 fabrics of experimental fault zones: Their development and relationship to mechanical behavior. In *Fault mechanics and transport properties of rocks*, B. Evans & T. B. T.-I. G. Wong (Eds.), (Vol. 51, pp. 33–67). Academic Press. https://doi.org/10.1016/S0074-6142(08)62814-4

Ma, S., Shimamoto, T., Yao, L., Togo, T., & Kitajima, H. (2014). A rotary-shear low to high-velocity friction apparatus in Beijing to study rock friction at plate to seismic slip rates. *Earthquake Science*, *27*(5), 469–497. https://doi.org/10.1007/s11589-014-0097-5

Marone, C. (1998). LABORATORY-DERIVED friction laws and their application to seismic faulting. *Annual Review of Earth and Planetary Sciences*, *26*(1), 643–696. https://doi.org/10.1146/annurev.earth.26.1.643

Marone, C., Raleigh, C. B., & Scholz, C. H. (1990). Frictional behavior and constitutive modeling of simulated fault gouge. *Journal of Geophysical Research*, *95*(B5), 7007–7025. https://doi.org/10.1029/JB095iB05p07007

Masoch, S., Fondriest, M., Gomila, R., Jensen, E., Mitchell, T. M., Cembrano, J., et al. (2022). Along-strike architectural variability of an exhumed crustal-scale seismogenic fault (Bolfin Fault Zone, Atacama Fault System, Chile). *Journal of Structural Geology*, *165*, 104745. https://doi.org/10.1016/j.jsg.2022.104745

Mizoguchi, K., Hirose, T., Shimamoto, T., & Fukuyama, E. (2007). Reconstruction of seismic faulting by high-velocity friction experiments: An example of the 1995 Kobe earthquake. *Geophysical Research Letters*, *34*(1), L01308. https://doi.org/10.1029/2006GL027931

Mizoguchi, K., Hirose, T., Shimamoto, T., & Fukuyama, E. (2009). Fault heals rapidly after dynamic weakening. *Bulletin of the Seismological Society of America*, *99*(6), 3470–3474. https://doi.org/10.1785/0120080325

Nielsen, S., Spagnuolo, E., Smith, S. A. F., Violay, M., Di Toro, G., & Bistacchi, A. (2016). Scaling in natural and laboratory earthquakes. *Geophysical Research Letters*, *43*(4), 1504–1510. https://doi.org/10.1002/2015GL067490

Nielsen, S., Spagnuolo, E., & Violay, M. (2012). Composite SAmple MOunt assembly (SAMOA): The ultimate sample preparation for rotary shear experiments.

Nielsen, S., Spagnuolo, E., Violay, M., & Di Toro, G. (2021). Thermal weakening friction during seismic slip: Experiments and models with heat sources and sinks. *Journal of Geophysical Research: Solid Earth*, *126*(5). https://doi.org/10.1029/2020JB020652

Nielsen, S., Spagnuolo, E., Violay, M., Smith, S., Di Toro, G., & Bistacchi, A. (2016). G: Fracture energy, friction and dissipation in earthquakes. *Journal of Seismology*, *20*(4), 1187–1205. https://doi.org/10.1007/s10950-016-9560-1

Niemeijer, A., Di Toro, G., Nielsen, S., & Di Felice, F. (2011). Frictional melting of gabbro under extreme experimental conditions of normal stress, acceleration, and sliding velocity. *Journal of Geophysical Research*, *116*(B7), B07404. https://doi.org/10.1029/2010JB008181

Noël, C., Giorgetti, C., Scuderi, M. M., Collettini, C., & Marone, C. (2023). The effect of shear displacement and wear on fault stability: Laboratory constraints. *Journal of Geophysical Research: Solid Earth*, *128*(4), e2022JB026191. https://doi.org/10.1029/2022JB026191

Ohnaka, M. (2003). A constitutive scaling law and a unified comprehension for frictional slip failure, shear fracture of intact rock, and earthquake rupture. *Journal of Geophysical Research*, *108*(B2), 1–21. https://doi.org/10.1029/2000JB000123

Ohnaka, M. (2013). Laboratory-derived constitutive relations for shear failure. In M. Ohnaka (Ed.), *The physics of rock failure and earthquakes* (pp. 28–90). Cambridge University Press. https://doi.org/10.1017/CBO9781139342865.004

Ohnaka, M., Akatsu, M., Mochizuki, H., Odedra, A., Tagashira, F., & Yamamoto, Y. (1997). A constitutive law for the shear failure of rock under lithospheric conditions. *Tectonophysics*, *277*(1), 1–27. https://doi.org/10.1016/S0040-1951(97)00075-9

Ohnaka, M., & Shen, L. (1999). Scaling of the shear rupture process from nucleation to dynamic propagation: Implications of geometric irregularity of the rupturing surfaces. *Journal of Geophysical Research*, *104*(B1), 817–844. https://doi.org/10.1029/1998JB900007

Ohnaka, M., & Yamashita, T. (1989). A cohesive zone model for dynamic shear faulting based on experimentally inferred constitutive relation and strong motion source parameters. *Journal of Geophysical Research*, *94*(B4), 4089–4104. https://doi.org/10.1029/JB094iB04p04089

Palmer, A. C., & Rice, J. R. (1973). The growth of slip surfaces in the progressive failure of over-consolidated clay. *Proceedings of the Royal Society of London. A. Mathematical and Physical Sciences*, *332*(1591), 527–548. https://doi.org/10.1098/rspa.1973.0040

Platt, J. D., Brantut, N., & Rice, J. R. (2015). Strain localization driven by thermal decomposition during seismic shear. *Journal of Geophysical Research: Solid Earth*, *120*(6), 4405–4433. https://doi.org/10.1002/2014JB011493

Platt, J. D., Rudnicki, J. W., & Rice, J. R. (2014). Stability and localization of rapid shear in fluid-saturated fault gouge: 2. Localized zone width and strength evolution. *Journal of Geophysical Research: Solid Earth*, *119*(5), 4334–4359. https://doi.org/10.1002/2013JB010711

Pozzi, G., De Paola, N., Holdsworth, R. E., Bowen, L., Nielsen, S. B., & Dempsey, E. D. (2019). Coseismic ultramylonites: An investigation of nanoscale viscous flow and fault weakening during seismic slip. *Earth and Planetary Science Letters*, *516*, 164–175. https://doi.org/10.1016/j.epsl.2019.03.042

Pozzi, G., De Paola, N., Nielsen, S. B., Holdsworth, R. E., & Bowen, L. (2018). A new interpretation for the nature and significance of mirror-like surfaces in experimental carbonate-hosted seismic faults. *Geology*, *46*(7), 583–586. https://doi.org/10.1130/G40197.1

Pozzi, G., De Paola, N., Nielsen, S. B., Holdsworth, R. E., Tesei, T., Thieme, M., & Demouchy, S. (2021). Coseismic fault lubrication by viscous deformation. *Nature Geoscience*, *14*(6), 437–442. https://doi.org/10.1038/s41561-021-00747-8

Proctor, B. P., Mitchell, T. M., Hirth, G., Goldsby, D., Zorzi, F., Platt, J. D., & Di Toro, G. (2014). Dynamic weakening of serpentinite gouges and bare surfaces at seismic slip rates. *Journal of Geophysical Research: Solid Earth*, *119*(11), 8107–8131. https://doi.org/10.1002/2014JB011057

Rempe, M., Di Toro, G., Mitchell, T. M., Smith, S. A. F., Hirose, T., & Renner, J. (2020). Influence of effective stress and pore fluid pressure on fault strength and slip localization in carbonate slip zones. *Journal of Geophysical Research: Solid Earth*, *125*(11), e2020JB019805. https://doi.org/10.1029/2020JB019805

Rempe, M., Mitchell, T., Renner, J., Nippress, S., Ben-Zion, Y., & Rockwell, T. (2013). Damage and seismic velocity structure of pulverized rocks near the San Andreas Fault. *Journal of Geophysical Research: Solid Earth*, *118*(6), 2813–2831. https://doi.org/10.1002/jgrb.50184

Rempe, M., Smith, S., Mitchell, T., Hirose, T., & Di Toro, G. (2017). The effect of water on strain localization in calcite fault gouge sheared at seismic slip rates. *Journal of Structural Geology*, *97*, 104–117. https://doi.org/10.1016/j.jsg.2017.02.007

Rempe, M., Smith, S. A. F., Ferri, F., Mitchell, T. M., & Di Toro, G. (2014). Clast-cortex aggregates in experimental and natural calcite-bearing fault zones. *Journal of Structural Geology*, *68*, 142–157. https://doi.org/10.1016/j.jsg.2014.09.007

Rempel, A. W., & Rice, J. R. (2006). Thermal pressurization and onset of melting in fault zones. *Journal of Geophysical Research*, *111*(B9), B09314. https://doi.org/10.1029/2006JB004314

Rice, J. R. (2006). Heating and weakening of faults during earthquake slip. *Journal of Geophysical Research*, *111*(B5). https://doi.org/10.1029/2005JB004006

Rodriguez-Navarro, C., Kudlacz, K., & Ruiz-Agudo, E. (2012). The mechanism of thermal decomposition of dolomite: New insights from 2D-XRD and TEM analyses. *American Mineralogist*, *97*(1), 38–51. https://doi.org/10.2138/am.2011.3813

Sibson, R. H. (1977). Fault rocks and fault mechanisms. *Journal of the Geological Society*, *133*(3), 191–213. https://doi.org/10.1144/gsjgs.133.3.0191

Sibson, R. H. (1989). Earthquake faulting as a structural process. *Journal of Structural Geology*, *11*(1–2), 1–14. https://doi.org/10.1016/0191-8141(89)90032-1

Sibson, R. H. (2003). Thickness of the seismic slip zone. *Bulletin of the Seismological Society of America*, *93*(3), 1169–1178. https://doi.org/10.1785/0120020061

Smith, S. A. F., Billi, A., Toro, G. D., & Spiess, R. (2011). Principal slip zones in limestone: Microstructural characterization and implications for the seismic cycle (tre monti fault, central apennines, Italy). *Pure and Applied Geophysics*, *168*(12), 2365–2393. https://doi.org/10.1007/s00024-011-0267-5

Smith, S. A. F., Di Toro, G., Kim, S., Ree, J.-H., Nielsen, S., Billi, A., & Spiess, R. (2013). Coseismic recrystallization during shallow earthquake slip. *Geology*, *41*(1), 63–66. https://doi.org/10.1130/G33588.1

Smith, S. A. F., Nielsen, S., & Di Toro, G. (2015). Strain localization and the onset of dynamic weakening in calcite fault gouge. *Earth and Planetary Science Letters*, *413*, 25–36. https://doi.org/10.1016/j.epsl.2014.12.043

Spagnuolo, E., Plümper, O., Violay, M., Cavallo, A., & Di Toro, G. (2015). Fast-moving dislocations trigger flash weakening in carbonate-bearing faults during earthquakes. *Scientific Reports*, *5*(1), 16112. https://doi.org/10.1038/srep16112

Tinti, E., Bizzarri, A., & Cocco, M. (2005). Modeling the dynamic rupture propagation on heterogeneous faults with rate- and state-dependent friction. *Annals of Geophysics*, *48*(2), 327–345. https://doi.org/10.4401/ag-3205

Tisato, N., Di Toro, G., De Rossi, N., Quaresimin, M., & Candela, T. (2012). Experimental investigation of flash weakening in limestone. *Journal of Structural Geology*, *38*, 183–199. https://doi.org/10.1016/j.jsg.2011.11.017

Tsutsumi, A., & Shimamoto, T. (1997). High-velocity frictional properties of gabbro. *Geophysical Research Letters*, *24*(6), 699–702. https://doi.org/10.1029/97GL00503

Tullis, T. E. (2015). Mechanisms for friction of rock at earthquake slip rates. In *Treatise on geophysics* (pp. 139–159). Elsevier. https://doi.org/10.1016/B978-0-444-53802-4.00073-7

Violay, M., Nielsen, S., Spagnuolo, E., Cinti, D., Di Toro, G., & Di Stefano, G. (2013). Pore fluid in experimental calcite-bearing faults: Abrupt weakening and geochemical signature of co-seismic processes. *Earth and Planetary Science Letters*, *361*, 74–84. https://doi.org/10.1016/j.epsl.2012.11.021

Wang, W., & Scholz, C. H. (1994). Micromechanics of the velocity and normal stress dependence of rock friction. *Pure and Applied Geophysics PAGEOPH*, *143*(1–3), 303–315. https://doi.org/10.1007/BF00874333

Yao, L., Ma, S., Platt, J. D., Niemeijer, A. R., & Shimamoto, T. (2016). The crucial role of temperature in high-velocity weakening of faults: Experiments on gouge using host blocks with different thermal conductivities. *Geology*, *44*(1), 63–66. https://doi.org/10.1130/G37310.1

Yao, L., Ma, S., Shimamoto, T., & Togo, T. (2013). Structures and high-velocity frictional properties of the Pingxi fault zone in the Longmenshan fault system, Sichuan, China, activated during the 2008 Wenchuan earthquake. *Tectonophysics*, *599*, 135–156. https://doi.org/10.1016/j.tecto.2013.04.011